Received: 27 April 2018 | Accepted: 17 September 2018

DOI: 10.1111/jmg.12454

ORIGINAL ARTICLE

WILEY Journal of METAMORPHIC GEOLOGY

A comparison of observed and thermodynamically predicted phase equilibria and mineral compositions in mafic granulites

Jacob B. Forshaw[1] | **David J. Waters**[1,2] | **David R. M. Pattison**[3] | **Richard M. Palin**[4] | **Phillip Gopon**[1]

[1]Department of Earth Sciences, University of Oxford, Oxford, UK

[2]Oxford University Museum of Natural History, Oxford, UK

[3]Department of Geoscience, University of Calgary, Calgary, AB, Canada

[4]Department of Geology and Geological Engineering, Colorado School of Mines, Golden, Colorado

Correspondence
Jacob B. Forshaw, Department of Geoscience, University of Calgary, Calgary, AB, Canada.
Email: jacob.forshaw1@ucalgary.ca

Present address
Jacob B. Forshaw, Department of Geoscience, University of Calgary, Calgary, AB, Canada.

Funding
Funding for this work was provided by the University of Oxford, Department of Earth Sciences as part of an MEarthSci thesis prepared by J.B. Forshaw under the supervision of D.J. Waters. Natural Sciences and Engineering Research Council of Canada (Discovery Grant 037233 to D.R.M Pattison).
Handling Editor: Richard White

Abstract

Recently published activity–composition (*a–x*) relations for minerals in upper amphibolite- and granulite facies intermediate and basic rocks have expanded our ability to interpret the petrological evolution of these important components of the lower continental crust. If such petrological modelling is to be reliable, the abundances and compositions of phases calculated at the interpreted conditions of metamorphic equilibration should resemble those in the sample under study. Here, petrological modelling was applied to six granulite facies rocks that formed in different tectonic environments and reached different peak metamorphic pressure–temperature (*P–T*) conditions. While phase assemblages matching those observed in each sample can generally be calculated at *P–T* conditions that approximate those of peak metamorphism, a consistent discrepancy was found between the calculated and observed compositions of amphibole and clinopyroxene. In amphibole, Si, Ca and A-site K are underestimated by the model, while Al and A-site Na are overestimated; comparatively, in clinopyroxene, Mg and Si are generally underestimated, while Fe^{2+} and Al are typically overestimated, compared to observed values. One consequence is a reversal in the Fe–Mg distribution coefficient (K_D) between amphibole and clinopyroxene compared to observations. Some of these mismatches are attributed to the incorrect partitioning of elements between the predicted amphibole and clinopyroxene compositions; however, other discrepancies are the result of the incorrect prediction of major substitution vectors in amphibole and clinopyroxene. These compositional irregularities affect mineral modal abundance estimates and in turn the position and size (in *P–T* space) of mineral assemblage fields, the effect becoming progressively more marked as the modal abundance of hornblende increases; hence, this study carries implications for estimating *P–T* conditions of high-temperature metabasites using these new *a–x* relations.

KEYWORDS
activity–composition relations, amphibole, clinopyroxene, granulite facies, metabasite

1 | INTRODUCTION

Rocks of broadly basic composition are important petrological constituents of both oceanic and continental crust, and may experience intense deformation and metamorphism during tectonic activity (Brown, 2007). During collisional orogenesis, elevated pressure (*P*) and temperature (*T*) conditions in the middle to lower continental crust can lead to

partial melting (England & Thompson, 1986). If enough melt is generated, it can separate from its source, ascend to higher crustal levels, and form felsic igneous intrusions, leaving behind a more mafic residue (Brown, 2013; Brown & Fyfe, 1970; Diener, White, & Hudson, 2014; Sawyer, 1994, 2001; White, Powell, & Clarke, 2002). As such, crustal anatexis facilitates long-term differentiation of the continental crust and granulitization of its lowermost levels (e.g. Daczko, Clarke, & Klepeis, 2001). A powerful technique for constraining the prograde and retrograde tectonothermal evolution of metamorphic rocks is comparison of the modes, compositions and textures of natural rocks with calculated phase equilibria on petrogenetic grids or rock-specific equilibrium phase diagrams, the latter commonly referred to as "pseudosections" (Powell & Holland, 2008; Powell, Holland, & Worley, 1998). However, until recently, appropriate thermodynamic models for complex solid solutions and melts applicable to mafic bulk compositions that have undergone granulite facies metamorphism have not been available.

Green et al. (2016) introduced activity–composition (a–x) relations for silicate melt of broadly trondhjemitic–tonalitic composition, augitic clinopyroxene with Si–Al mixing on the tetrahedral sites, and amphibole that incorporates K_2O and TiO_2 into the formula unit. In a companion study to that work, Palin, White, et al. (2016) used these a–x relations to investigate phase equilibria in generic basic and intermediate lithologies, including modern-day mid-ocean ridge basalt (MORB) and diorite. They showed that the calculated mineral assemblages and modal proportions generally produced good matches with those reported from granulite facies rocks of these compositions. However, modelling was not completed for specific naturally occurring rocks; hence, there was no direct comparison against petrologically observed mineral abundances and mineral chemical analyses.

The ultimate aim is to conduct thermobarometry using the approach of Powell and Holland (2008), in which compositional isopleths of major phases intersect in the correct assemblage field, and in turn, a close relationship is found between natural and calculated phase compositions. If these conditions are met, then the models can be used for self-consistent P–T determination, whereby all equilibria used are founded from the same data set. This type of analysis is important for mafic lithologies that have calculated assemblage fields spanning large ranges in P–T space, in which compositional changes in the minerals (e.g. amphibole, plagioclase, and pyroxenes) are the primary indicators of different P–T conditions.

In this paper, we examine how closely thermodynamically predicted phase assemblages, modes, and mineral compositions match those observed in six natural high-grade metabasic rocks that reached a variety of peak P–T conditions and formed in different tectonic settings. These comprise (a) two samples of hornblende–granulite from the regionally metamorphosed Namaqualand Metamorphic Complex, South Africa; (b) a hornblende and biotite-bearing mafic migmatite from Cone Peak in the Santa Lucia continental arc, California, USA; (c) a two-pyroxene granulite from the Archean Lewisian Complex, northwest Scotland, UK; and (d) two samples of garnet granulite from the Kapuskasing Structural Zone, Ontario, Canada. While modelled assemblages are generally similar to those observed, consistent discrepancies were found between predicted and measured compositions of amphibole and clinopyroxene, and consequently, for the modal proportions of these phases. We discuss potential causes of these discrepancies and the implications they have for phase equilibrium modelling of high-grade metabasic rocks.

2 | SAMPLE, MINERAL, AND ANALYSIS CONSIDERATIONS

2.1 | Sample selection

Granulite facies rocks were chosen from four regions representing a range of pressures, temperatures, and hydrous mineral contents. By using samples held in collections at the University of Oxford, UK, and University of Calgary, Canada, we were able to determine that thin sections and hand specimens were representative of outcrops through consultation with the original field geologists and comparison with field photographs. Many of the rocks from these high-T environments are migmatitic; however, to avoid complications from heterogeneity, the modelling was conducted on macroscopically homogeneous rock volumes that lack quartzofeldspathic segregations (leucosomes) commonly associated with melt generation, such as the mesosome/palaeosome regions of migmatitic rocks, or the nonmigmatitic domains of metabasic horizons (Waters, 1988).

2.2 | Microprobe analysis

Mineral compositions from four of the six studied samples were obtained on a CAMECA SXFive field-emission electron probe micro-analyser (EPMA) equipped with wavelength-dispersive spectrometers, located in the Department of Earth Sciences, University of Oxford, UK. Operating conditions included an acceleration voltage of 15 kV, a beam current of 20 nA, and a spot size of 1 μm. An X-phi matrix correction for atomic number, absorption, and fluorescence was automatically applied to all analyses. The potential for calibration error was mitigated by recalibrating before each session against a range of natural and synthetic standards.

Multiple spot analyses and line profiles were taken across pyroxene, amphibole, plagioclase, garnet, and biotite

grains in each sample to determine the extent of intracrystalline compositional variation. By analysing the same mineral phase in different parts of each thin section, it was possible to determine the amount of intergrain heterogeneity within and between thin sections. The locations of all mineral analyses in thin sections were chosen randomly (i.e., no bias) from well-polished, unblemished areas of unaltered grains. Mineral composition data for samples SA1-4a and SA1-13, from the Kapuskasing Structural Zone, were taken from tables 1 to 4 of Hartel and Pattison (1996).

2.3 | Mineral formula recalculation

Electron probe microanalyser-derived mineral compositional analyses (in wt% oxide) were converted to molecular mineral formulae using a standard number of oxygen atoms per formula unit. Amphibole, represents one exception to this scheme, with a 23-oxygen +Ti cations/2 formula unit being used and H_2O content defined as (2-Ti)OH; this change was made to emulate the amphibole *a–x* relation of Green et al. (2016). Biotite represents another exception where a 22-oxygen +Ti cation recalculation is used, due to the high Ti contents of granulite facies biotite (Waters & Charnley, 2002). The proportion of Fe^{3+} in pyroxene and garnet was determined using the method of Droop (1987), and that in amphibole was determined using the technique of Holland and Blundy (1994). Since there is no readily available method of calculating the Fe^{3+} in biotite, 11% of the total measured Fe was assumed to be Fe^{3+}. This value was taken from Mössbauer spectroscopy determinations of biotite in metapelitic rocks (Guidotti & Dyar, 1991) in the absence of equivalent experiments conducted for biotite in high-*T* metabasites. This 11% estimate likely represents a minimum because of the presence of magnetite in the metabasic granulite samples reported here.

Error propagation of measured data through formula recalculation was performed to determine the uncertainty on cation numbers and other derived values, for comparison against calculated values. Standard deviations on oxide weight percentages were estimated for each element from counting statistics, guided by the *SD* measured on the weight per cent total of a homogeneous population of analyses. These uncertainties were propagated through formula recalculations for amphiboles and pyroxenes using a Monte Carlo method that employed Gaussian perturbations on the raw oxide weight per cent to estimate 2σ values for cations and site occupancies. This is particularly important for estimating the increased uncertainty on cations that are distributed over more than one site, or for estimates of ferric iron. As a result, all quoted cation proportions and other derived values in Section 3 have associated ±2σ values stated alongside them.

Special considerations arise for the comparison of analysed minerals with model calculations in the case of hornblende and clinopyroxene. In high-*T* hornblende, two major compositional unknowns are the ferric iron content and the extent to which high-charge cations in octahedral sites (e.g. Ti^{4+}, Fe^{3+}) are accommodated by deprotonation (oxy-) substitutions (e.g. Popp & Bryndzia, 1992). Recalculation schemes such as that of Holland and Blundy (1994) bracket the likely values of Fe^{3+} using stoichiometric criteria, choosing a mean value between the stoichiometric limits as the best estimate. In most cases, for the high-*T* calcic amphibole in this study (1.83–1.91 Ca per formula unit), the limits satisfy the requirement for Ca to occur only on M4 sites. At the lower limit for Fe^{3+}, corresponding to a higher cation total for a given anion charge, Ca and other non-alkali cations total 15, there is no Na on M4, and the amount of Fe^{2+}+Mg on M4 (cummingtonite/grunerite) is maximized. Conversely, at the upper limit for Fe^{3+}, Na in M4 is maximized, and no Fe^{2+} or Mg is located on M4. Since neither of these limiting cases is petrologically likely, the mean value for Fe^{3+}, and its *SD* in a population of stoichiometric amphibole analyses, was taken as a reasonable estimate of the ferric iron content. The Fe^{3+} estimates obtained in this way have been shown to be in reasonable agreement with wet chemical and Mössbauer determinations on similar granulite facies hornblende (Cosca, Essene, & Bowman, 1991; Haynes, 1998). The effect of varying the anion charge as a result of deprotonation substitutions was also investigated by calculating cation distributions in the natural hornblende at a range of OH contents. The principal result of increasing anion charge is to increase the Fe^{3+} content without significantly affecting the site occupancies. For consistency, the hornblende has been recalculated on the same basis as that in the Green et al. (2016) *a–x* relation, in which half of the Ti substitution is taken to involve deprotonation. In conjunction with the Holland and Blundy (1994) scheme, this yields estimates of Fe^{3+} content that are in reasonable agreement with model values, demonstrating that no significant bias is introduced into the patterns of occupancy of other cations that might affect the comparisons to be discussed later. No correction was made to the natural amphibole formulae for the small amount of Mn (0.10–0.30 wt% MnO).

The clinopyroxene examined in this study contains Ti (0.20–0.50 wt% TiO_2) and Mn (0.15–0.50 wt% MnO) in addition to the elements considered in the *a–x* relation. Instead of disregarding these small amounts, the clinopyroxene compositions were projected from the relevant Ti and Mn end-member compositions. The samples show strong positive correlations between Ti and Al cations, suggesting that an appropriate Ti end-member is $CaTiAl_2O_6$ (Loucks, 1990; Morimoto, 1988). Therefore, projection reduced the Al content of the clinopyroxene

relative to the raw analyses. Clinopyroxene was also projected from johannsenite ($CaMnSi_2O_6$) to eliminate MnO. None of the analysed pyroxene contained measurable K_2O.

Mean weight per cent oxide analyses and calculated cations per formula unit (cpfu) are presented in Tables S1–S6. The following phases appear in the text and figures: melt (L), hornblende (hb), augite (aug), orthopyroxene (opx), garnet (g), plagioclase (pl), K-feldspar (ksp), biotite (bi), epidote (ep), ilmenite (ilm), hematite (hem), magnetite (mt), spinel (sp), rutile (ru), titanite (sph), and quartz (q). All phase abbreviations are consistent with those of Holland and Powell (2011) and Green et al. (2016). End-member nomenclature and elemental site allocations for clinopyroxene and amphibole are taken from Morimoto (1988) and Leake et al. (1997, 2003) respectively. The vector treatment of Schumacher (2007) was also applied to amphiboles to provide a clear representation of analyses within amphibole compositional space.

2.4 | Mineral abundance estimates

Mineral proportions in natural samples were calculated using JMicroVision (Roduit, 2016), by point counting high-resolution scans of entire thin sections. In most cases, minerals were optically distinct, but for quartz/plagioclase and the iron oxide phases, estimates were made based on point counting a typical area of a composition map obtained via EPMA. By combining these phase percentages (Table S7) with their representative compositions, a bulk composition was determined (described in Section 4). Factors that contribute to uncertainty in point counted estimates include the amount of the mineral, its grain size and shape, its spacing between points, and the number of points counted. The main contribution to this error is the relationship between amount of a mineral present and number of points counted (Van der Plas & Tobi, 1965). For the samples considered herein, 500 randomly distributed points were counted for each thin section, which produces 2σ relative uncertainties of ~8% for minerals with volumes greater than 50 vol.% (equal to an absolute uncertainty of ~4%), and relative uncertainties up to ~20% for minerals with volumes less than 10 vol.% (absolute uncertainty of ~2 vol.%; Van der Plas & Tobi, 1965). While these values may appear large for the purposes of this study, because thin sections represent two-dimensional slices through naturally heterogeneous three-dimensional rocks, there is inherent information loss associated with calculating mineral proportions in this way, regardless of how many points are used. Nonetheless, by constructing the bulk composition for each sample from these data, the calculated phase diagram should always be representative of this two-dimensional slice.

3 | REGIONAL SETTINGS, SAMPLE PETROLOGY, AND MINERAL CHEMISTRY

3.1 | DWN-346 and DWN-362: Namaqualand Metamorphic Complex, South Africa

The Namaqualand Metamorphic Complex forms part of a Proterozoic orogenic belt on the southern margin of the Kaapvaal craton in southern Africa (Colliston, Schoch, & Cole, 2014; Hartnady, Joubert, & Stowe, 1985). It experienced high-grade, granulite facies metamorphism at 1,030–1,040 Ma during the Namaqua thermal event (Robb, Armstrong, & Waters, 1999). Samples DWN-346 and DWN-362 presented in this work were collected from a belt of granulite facies supracrustal gneisses exposed in the Buffels River region of the Bushmanland subprovince. The sampling area falls in the northern zone B of fig. 1b in Waters (1989), with more detailed geological descriptions given in Waters and Moore (1985) and McStay (1991). Mafic granulites in this locality represent the metamorphosed remnants of volcanic horizons and sills that intruded into semipelitic and pelitic gneisses (McStay, 1991). Thermobarometry performed on these host metasedimentary rocks suggested that the entire sequence reached at least 800°C at a well-constrained pressure of 5.5 kbar (Waters, 1989).

DWN-346 was sampled from near the margin of a 20-m-thick unit; it has a microstructure of poikiloblastic pyroxene replacing amphibole (Figure 1a), interpreted by Waters (1988) to result from dehydration of hornblende under the influence of a gradient in chemical potential of H_2O between the mafic rock and adjacent semipelitic migmatites. DWN-362 was taken from a thin, 10 cm sheet in migmatitic metapelites; this sample exhibits an anhydrous two-pyroxene granulite at its margins, grading into a hornblende-bearing domain in the centre of the layer (Figures 1b and 2b). Both samples contain the mineral assemblage clinopyroxene, orthopyroxene, amphibole, plagioclase, magnetite, ilmenite, and quartz; DWN-346 additionally contains minor biotite.

All analysed minerals except for plagioclase exhibit largely homogeneous compositions, with no substantial variation within or between the samples. Plagioclase had the greatest variety of compositions within and between samples, with X_{An} (=Ca/(Ca+Na+K) = 0.65 ± 0.05 and 0.90 ± 0.02 in DWN-346 and DWN-362 respectively. Orthopyroxene in DWN-346 has X_{Mg} (=Mg/Mg+Fe^{2+}) = 0.66 ± 0.01 and Al = 0.05 ± 0.01 cpfu, while in DWN-362, it has X_{Mg} = 0.61 ± 0.01 and Al = 0.06 ± 0.01 cpfu. In DWN-346, clinopyroxene displays X_{Mg} = 0.77 ± 0.03, Na = 0.03 cpfu, Al = 0.09 ± 0.01 cpfu, and Ca = 0.91 ± 0.04 cpfu,

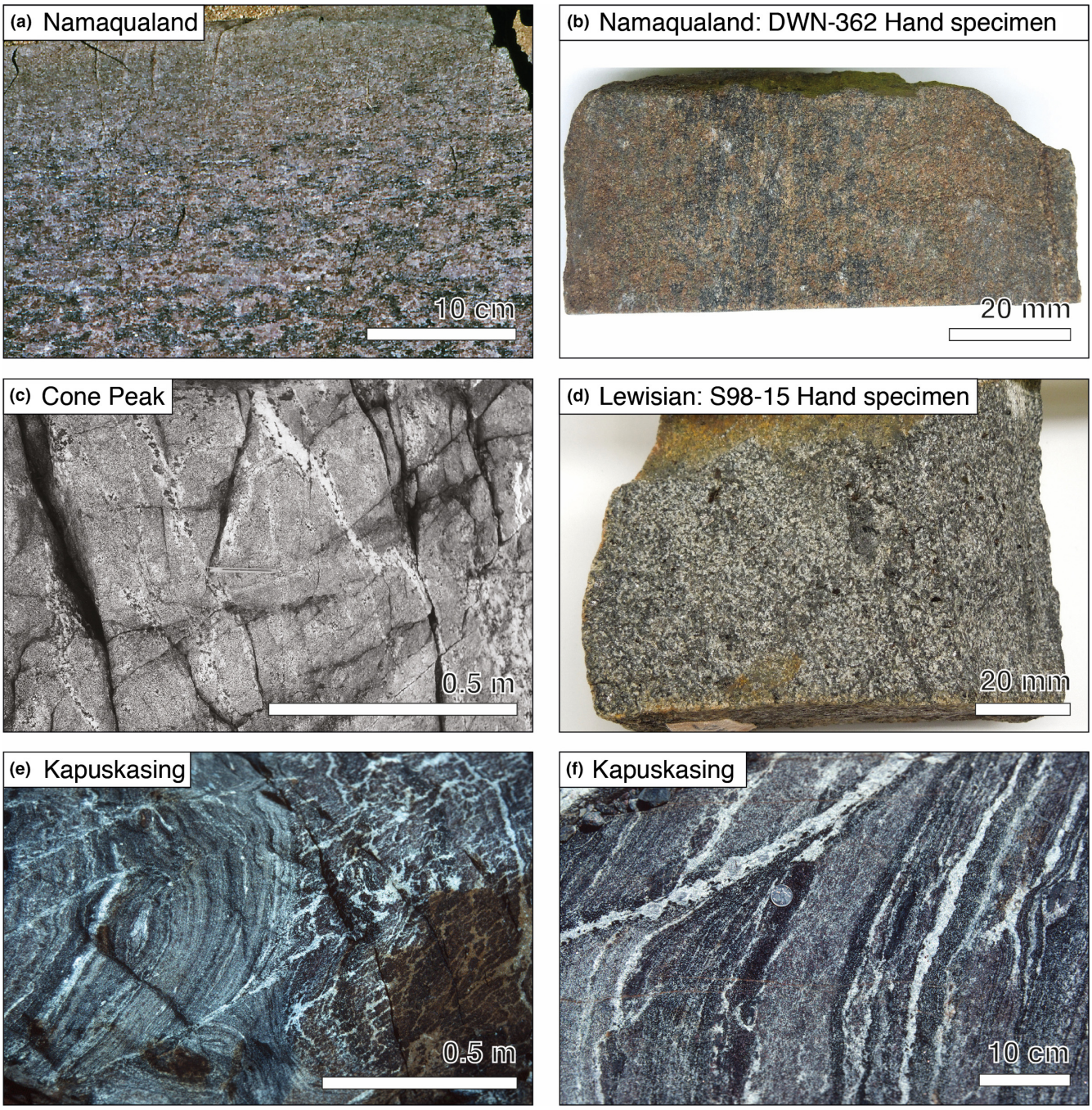

FIGURE 1 Outcrop and hand specimen photos showing representative textures for each of the studied samples. (a) Coarse brown poikiloblastic orthopyroxene and clinopyroxene patches overprinting granoblastic amphibolite. (b) Hand specimen of DWN-362 exhibiting the dehydrated margins of the 10 cm sheet and central remanent amphibole. (c) Representative photo from Cone Peak of the orthopyroxene-bearing pervasive leucocratic veins that separate regions of biotite–hornblende-bearing host rock. (d) Hand specimen of S98-15 showing pyroxene, plagioclase, and minor biotite. (e) Representative photo from Kapuskasing detailing the relatively more abundant nature of the pervasive leucocratic veins in the amphibolite (right) compared to the clinopyroxene-rich layers (left). (f) Photo distinguishing the dark hornblende-rich domains (SA1-13) and the relatively more anhydrous, light-coloured, garnet–augite-rich regions (SA1-4a)

classifying as diopside–augite. Comparatively, clinopyroxene in DWN-362 has $X_{Mg} = 0.75 \pm 0.05$, Na = 0.04 ± 0.01 cpfu, Al = 0.09 ± 0.02 cpfu, and Ca = 0.89 ± 0.06 cpfu, also classifying as diopside–augite. Amphibole in DWN-346 has Si = 6.55 ± 0.06 cpfu, Na = 0.37 ± 0.05 cpfu, K = 0.29 ± 0.02 cpfu, Ti = 0.23 ± 0.02 cpfu, and $X_{Mg} = 0.70 \pm 0.03$, classifying as potassian-pargasite, while in DWN-362, it has Si = 6.53 ± 0.12 cpfu, Na = 0.35 ± 0.04 cpfu, K = 0.22 ± 0.03 cpfu, Ti = 0.14 ± 0.01 cpfu, and $X_{Mg} = 0.76 \pm 0.03$, classifying as pargasite.

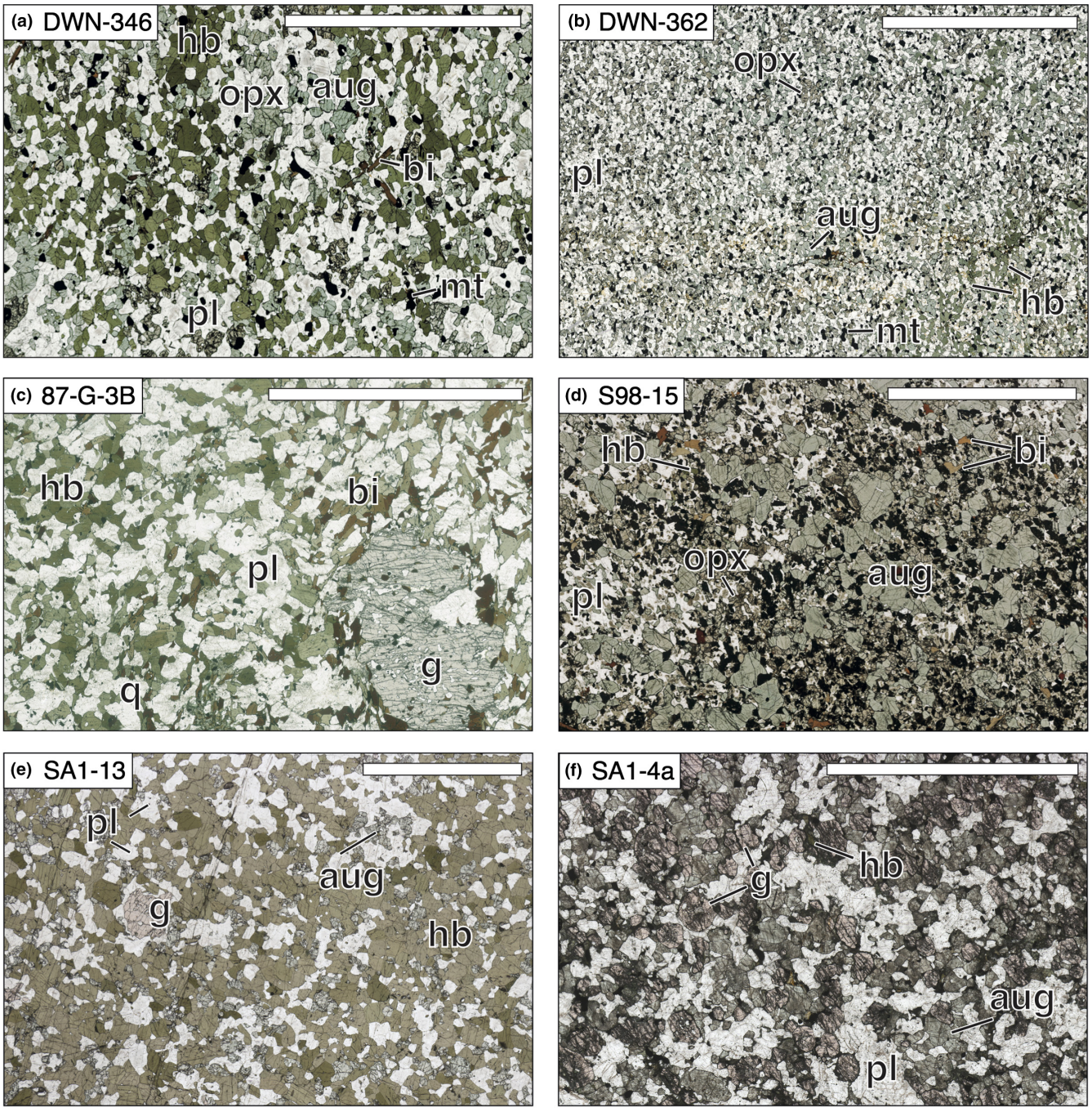

FIGURE 2 Plane polarized light photomicrographs of key petrological features in the studied samples. Scale bars = 10 mm (a) DWN-346 contains a texturally equilibrated matrix of hornblende, orthopyroxene, augite, and plagioclase, with minor biotite and magnetite distributed throughout. (b) The relatively finer grained DWN-362 exemplifies gradation from a dehydrated augite and orthopyroxene rim to hornblende-bearing right hand-side. (c) 87-G-3B shows a large homogeneous garnet in a matrix of amphibole, biotite, plagioclase, and quartz. (d) S98-15 depicts the augite crystals in a finer matrix of plagioclase, orthopyroxene, biotite, and hornblende, listed in decreasing order of abundance. (e) SA1-13 exhibits relatively smaller garnet porphyroblasts in a matrix of granoblastic polygonal hornblende, plagioclase, and diopside. (f) SA1-4a contains a granoblastic polygonal matrix of garnet, augite, and plagioclase with minor hornblende

3.2 | 87-G-3B: Cone Peak, California, USA

The summit of Cone Peak in the Santa Lucia Range, California, exposes a high-grade metamorphic–plutonic complex, within the fault-bound Salinian block (Hansen & Harlov, 2009; Hansen & Stuk, 1993; Ross, 1976). The rocks are abundant granulite facies migmatites (Compton, 1960) that formed from high-grade metamorphism and partial melting of a hornblende- and biotite-bearing diorite protolith at *c.* 100–105 Ma (Mattinson, 1978), contemporaneous with

plutonic activity in the region. For a detailed description of the regional geology, structure, and age relationships in the region, the reader is referred to Compton (1966) and Kidder, Ducea, Gehrels, Patchett, and Vervoort (2003). Hansen and Stuk (1993) used conventional geothermobarometry to obtain an estimate of peak metamorphic temperature and pressure in the range 700–750°C and 7.0–7.5 kbar.

In outcrop, relatively homogeneous meta-diorite is transected by discrete veins of orthopyroxene-bearing leucocome (Figure 1c), with biotite-enriched selvedges separating the two domains. Hansen and Stuk (1993) attributed the formation of these orthopyroxene-bearing migmatites to partial melting of a homogeneous rock in an open system, similar to the mechanism described by Pattison (1991) for granulite facies metagabbros of the Grenville Province, Ontario, Canada. In this scenario, melting was promoted by the chemical interaction of a low-a(H_2O) fluid with the rocks, resulting in a change from infiltration-driven dehydration to infiltration-driven melting (Hansen & Stuk, 1993; Pattison, 1991). Specimen 87-G-3B represents an unmigmatized portion of meta-diorite, characterized by a granoblastic biotite–hornblende–plagioclase–quartz matrix with centimetre-scale garnet porphyroblasts (Figure 2c).

Electron microprobe analysis revealed that all matrix minerals show limited compositional variation; additionally, all ferromagnesian phases have $X_{Mg} < 0.5$, indicating the relatively high Fe content of the protolith. Plagioclase has $X_{An} = 0.39 \pm 0.02$; amphibole has Si = 6.28 ± 0.11 cpfu, Na = 0.41 ± 0.08 cpfu, K = 0.36 ± 0.03 cpfu, Ti = 0.30 ± 0.05 cpfu, and $X_{Mg} = 0.43 \pm 0.01$, classifying as potassian-ferropargasite; biotite has Ti = 0.73 ± 0.12 cpfu and Al = 2.70 ± 0.11 cpfu; garnet is dominantly almandine (63 ± 2%), with lesser grossular (20 ± 1%), pyrope (14 ± 1%), and spessartine (3 ± 1%) components.

3.3 | S98-15: Lewisian Complex, Scotland

The Archean Lewisian Complex in northwest Scotland comprises primarily tonalite–trondhjemite–granodiorite orthogneiss, with lesser amounts of metamorphosed mafic and ultramafic rocks (Johnson & White, 2011; Mason & Brewer, 2005; Park, 1966; Peach et al., 1907; Rollinson & Fowler, 1987; Rollinson & Windley, 1980; White, Palin, & Green, 2017). Sample S98-15 was collected from Scouriemore, in the Complex's "central region," which experienced (ultra)high-*T* metamorphism (Johnson & White, 2011) during the Badcallian regional metamorphic episode at *c.* 2,700–2,800 Ma (Love, Kinny, & Friend, 2004). Sills and Rollinson (1987) summarized the wide range of *P–T* estimates presented for Badcallian metamorphism in the central region, including evaluations <8 to >15 kbar and <800°C to >1,100°C. However, these results were obtained exclusively using conventional thermobarometry and thus some of the estimates may reflect the effects of down-temperature re-equilibration (cf. Frost & Chacko, 1989). More recent investigations that have used phase equilibrium modelling report tighter constraints on peak *P–T* conditions of ~8.0–11.5 kbar and 875–1,000°C, followed by near-isothermal decompression to pressures of 7.0–9.0 kbar (Feisel, White, Palin, & Johnson, 2018; Johnson & White, 2011).

Lewisian mafic granulites exposed at Scouriemore range from garnet–clinopyroxene rocks with minor plagioclase through to two-pyroxene granulites. S98-15, sampled from a metabasic granulite body on the northern coast, has a granoblastic texture with large (~2–5 mm) augite porphyroblasts and a matrix comprising smaller plagioclase, orthopyroxene, and magnetite grains (Figure 1d). Hornblende and biotite together account for less than 2% of the rock, with the former commonly included within pyroxene (Figure 2d). No garnet was observed in the polished thin section used for study here; however, in one of the five other thin sections taken from the same sample, small remnants of garnet are visible.

All minerals show minimal within-grain compositional variation: plagioclase is labradoritic ($X_{An} = 0.60 \pm 0.06$); orthopyroxene has $X_{Mg} = 0.56 \pm 0.01$ and Al = 0.12 ± 0.02 cpfu; clinopyroxene has $X_{Mg} = 0.72 \pm 0.03$, Na = 0.04 ± 0.01 cpfu, Al = 0.15 ± 0.04 cpfu, and Ca = 0.90 ± 0.04 cpfu, classifying as diopside–augite; amphibole has Si = 6.13 ± 0.09 cpfu, Na = 0.35 ± 0.04 cpfu, K = 0.49 ± 0.08 cpfu, Ti = 0.23 ± 0.07 cpfu, and $X_{Mg} = 0.60 \pm 0.03$, classifying as potassian-pargasite; biotite has Ti = 0.60 ± 0.01 cpfu and Al = 2.60 ± 0.05 cpfu.

3.4 | SA1-13 and SA1-4a: Kapuskasing Structural Zone, Ontario, Canada

The Kapuskasing Structural Zone, Ontario, exposes an oblique section through ~20 km of Archean crust, uplifted along a northwest-dipping thrust fault (Percival & Card, 1983). The highest grade rocks adjacent to the fault zone comprise layered, migmatitic, granulite facies mafic gneisses (Percival, 1983), formed between 2,660 and 2,640 Ma (Krogh, 1993); these range from garnet+clinopyroxene+plagioclase-rich gneisses to hornblende-rich gneisses, the latter with trondhjemitic leucosomes occurring as patches, veins, and dykes at a range of scales (Hartel & Pattison, 1996; see Figure 1d). Hartel and Pattison (1996) assessed peak conditions of metamorphism to lie in the 9–11 kbar and 700–850°C range, favouring an estimate of 11 kbar and 850°C based on comparison of the mineral assemblages with experimentally constrained phase equilibria.

At Kapuskasing, hornblende-rich layers typically exhibit a greater abundance of segregated leucosomes than clinopyroxene-rich layers (Figure 1e,f). Sample SA1-13 is a hornblende granulite collected from a leucosome-free

domain within a hornblende-rich layer. Comparatively, SA1-4a was taken from a hornblende-poor, clinopyroxene-rich layer. Both thin sections are texturally well equilibrated; SA1-13 has a matrix of mm-sized granoblastic polygonal hornblende, plagioclase, and clinopyroxene, alongside slightly larger porphyroblasts of garnet, while SA1-4a has mm-sized granoblastic plagioclase, clinopyroxene and garnet with minor hornblende (Figure 2e,f). Minor quartz and titanite appear in the matrix of both rocks, whilst, in SA1-13 specifically, titanite is also concentrated as inclusions in garnet.

Hartel and Pattison (1996) reported that plagioclase is the only mineral to show significant compositional variation in rocks from across the region, with the An content in hornblende-rich gneisses (39–47%) being intermediate between that in trondhjemitic leucosome (35–40%) and garnet–diopside–plagioclase-rich domains (43–80%). Slight variation in the X_{Mg} values at the rims of garnet, clinopyroxene, and hornblende was also noted. Mineral compositions in the two samples are very similar: plagioclase has an average X_{An} of 0.45 and 0.43 in SA1-13 and SA1-4a respectively; clinopyroxene ranges in X_{Mg} from 0.62 to 0.68 and has Na = 0.05 cpfu, Al = 0.12 cpfu, and Ca = 0.88 cpfu, classifying as diopside–augite; amphibole has Si = 6.28–6.33 cpfu, Na = 0.42–0.45 cpfu, K = 0.15–0.21 cpfu, Ti = 0.19 cpfu, and X_{Mg} = 0.49–0.55, classifying as pargasite and ferropargasite for SA1-13 and SA1-4a respectively; garnet is dominantly almandine (55%), with lesser grossular (25–29%), pyrope (12–14%), and spessartine (3–5%) components.

4 | PHASE EQUILIBRIUM MODELLING CONSIDERATIONS

The focus of this study is to determine the ability of recently published amphibole, clinopyroxene, and melt *a–x* relations (Green et al., 2016) to replicate mineral assemblages, modes, and mineral compositions in natural rocks. Therefore, the following section outlines the authors' approach to bulk composition calculation, phase equilibrium modelling, and *P–T* estimation, as well as the uncertainties associated with each of these, before detailing the comparison strategy used for testing the models.

4.1 | Bulk composition calculation

As bulk composition is the primary control on phase diagram topology and phase proportions/compositions in an equilibrium assemblage (e.g. Stüwe & Powell, 1995), care must be taken to determine the most appropriate effective bulk composition representing an equilibration volume at the *P–T* conditions of interest. Recent studies have quantified some of the issues involved with defining such a composition (e.g. Guevara & Caddick, 2016; Palin, Weller, Waters, & Dyck, 2016), and discussed the relative magnitudes of different sources of uncertainty. In Section 5.3, we consider the uncertainty associated with the calculated bulk compositions and the effect this has on the predicted phase assemblage and the modal abundance of minerals.

Effective bulk compositions for each sample were determined by combining phase proportions with their representative compositions (cf. Carson, Powell, & Clarke, 1999). This method was chosen over whole-rock X-ray fluorescence (XRF) due to concerns in these migmatitic rocks regarding sample heterogeneity and the extent to which an XRF bulk composition is appropriate for the volume represented by the thin section. Bulk rock H_2O and $X_{Fe^{3+}}$ contents were calculated using this same technique, based on the proportions of H_2O and $X_{Fe^{3+}}$ in each of the constituent minerals (as determined from recalculated EPMA data). Concerning H_2O, a consequence of this approach is that the lower temperature parts of the calculated phase diagrams are not appropriate for interpreting the natural mineral assemblage that developed during prograde metamorphism because H_2O in fluid or melt will have been lost during the rocks' evolution to the observed mineral assemblage. However, phase diagrams were designed only to locate the peak, or equilibrated, metamorphic assemblage and not to consider *P–T* paths. Additional components in hornblende or biotite, such as Cl or F, that would act to decrease overall bulk rock H_2O contents are not considered in our model system, since geochemical analyses of these phases for 87-G-3B (Hansen & Stuk, 1993) and SA1-13/SA1-4a (Hartel & Pattison, 1996) show these anions exist in negligible amounts. The effective bulk compositions used for modelling are presented in Table 1.

4.2 | Phase equilibrium modelling

Phase diagrams were constructed for each of the six samples, allowing examination of the predicted equilibrium phase proportions and compositions at and around the interpreted *P–T* conditions of formation. All calculations were completed in the 10-component NCKFMASHTO (Na_2O–CaO–K_2O–FeO–MgO–Al_2O_3–SiO_2–H_2O–TiO_2–O_2) system using THERMOCALC version 3.45i (Powell & Holland, 1988) and the internally consistent data set of Holland and Powell (2011) (update ds62, 6th February 2012). The following *a–x* relations were used: melt, augite, and hornblende (Green et al., 2016); garnet, orthopyroxene and biotite (White, Powell, Holland, Johnson, & Green, 2014); epidote (Holland & Powell, 2011); magnetite–spinel (White et al., 2002); ilmenite–hematite (White, Powell, Holland, & Worley, 2000); plagioclase (pl, $C\bar{1}$, and pli, $I\bar{1}$, the latter used when $X_{An} > 0.8$, consistent with Green et al. (2016)),

and K-feldspar (Holland & Powell, 2003). Pure phases included quartz, rutile, and titanite. Phase diagrams are shaded according to the variance of each field, with darker shades indicating higher variance.

4.3 | Identification of a stable assemblage field

Comparison between predicted and observed mineral proportions and compositions was carried out using the following methodology. First, the stability field representing the interpreted peak, or equilibrated, metamorphic mineral assemblage was identified on the phase diagram. If the phase diagram did not provide an exact match to the interpreted assemblage, the degree of discrepancy was assessed based on the relative proportions of minerals in the analysed samples. The most common discrepancies involved minerals of small modal abundance. For example, if a sample contained <1 vol.% ilmenite, and an interpreted assemblage field matched the observed assemblage with the exception of ilmenite, this field was taken to be representative of the rock as a whole, as such minor differences are well within the margins of error associated with this modelling technique (Guevara & Caddick, 2016; Palin, Weller, et al., 2016).

4.4 | *P–T* estimation

The *P–T* conditions experienced by the rocks establish the point of comparison between predicted and observed modes and mineral compositions. Estimating this *P–T* condition, however, is not straightforward, as recently alluded to in Huang, Brown, Guo, Piccoli, and Zhang (2018). One approach is to use conventional geothermobarometry, or multiequilibrium thermobarometric methods like av*PT* (Powell & Holland, 1994). However, the high metamorphic temperatures experienced by granulite facies rocks result in the likelihood of intracrystalline diffusional exchange on cooling from peak conditions, resulting in modifications of mineral compositions from those at peak conditions (Frost & Chacko, 1989; Pattison & Bégin, 1994). One common diffusional modification involves Fe and Mg, which are involved in simple exchange reactions among the Fe–Mg silicates pyroxene, garnet, amphibole and, where present, biotite. Even if the minerals are largely unzoned in Fe and Mg, or have broad plateau regions with little zoning, they could still have experienced modification of Fe–Mg ratios, as shown in the study of Pattison and Bégin (1994). Other elements like Ca, Al, and Si, are more commonly involved in net transfer reactions; they are also less mobile and hence less prone to diffusional modification, the result being different closure temperatures for different elements. These considerations mean that *P–T* estimates from these methods, are unlikely to be reliable. Independently calibrated conventional geothermobarometers present a further problem in that the thermodynamic data, or geothermobarometric formulations, that underpin the method are different from the thermodynamic data used in the phase equilibrium analysis in this paper, leading to potentially systematic discrepancies.

A second approach involves comparison of the observed mineral assemblages with experimental studies conducted on rocks of broadly similar composition. For example, Hartel and Pattison (1996) obtained *P–T* estimates for the Kapuskasing mafic migmatites by comparing the mineral assemblages with the mafic dehydration melting experiments of Patiño Douce and Beard (1995). This approach typically yields higher temperature estimates than from thermobarometry, generally closer to those derived from phase equilibrium modelling, but they are necessarily approximate because the natural rock compositions differ to some degree from the experimental compositions (Pattison, Chacko, Farquhar, & McFarlane, 2003).

TABLE 1 Bulk rock compositions used for phase diagram construction (mol.% oxide). FeO^{tot} is total iron expressed as FeO. O is oxygen, which combines with FeO via the equation $2FeO+O=Fe_2O_3$; hence, bulk O is identically equal to bulk Fe_2O_3, while true bulk FeO is given by $FeO^{tot}–2\times O$. Bulk rock $X_{Mg}=MgO/(MgO+FeO^{tot})$, and $X_{Fe^{3+}}=(2\times O)/FeO^{tot}$

Sample	Locality	Lithology	Figure	H_2O	SiO_2	Al_2O_3	CaO	MgO	FeO	K_2O	Na_2O	TiO_2	O	X_{Mg}	$X_{Fe^{3+}}$
DWN-346	Namaqualand	Hbl granulite	3a	1.39	47.13	9.53	13.74	11.18	11.55	0.34	2.05	0.71	2.39	0.49	0.41
DWN-362	Namaqualand	Hbl granulite	4a	0.67	43.81	9.30	14.16	10.47	16.46	0.09	0.55	0.66	3.84	0.39	0.47
87-G-3B	Cone Peak	Hbl–Bt granulite	5a	2.46	55.41	13.30	7.53	4.57	9.26	1.73	4.00	1.21	0.54	0.33	0.12
S98-15	Lewisian Complex	Granulite	6a	0.18	50.62	9.89	14.84	10.14	10.24	0.17	2.11	0.07	1.73	0.50	0.34
SA1-13	Kapuskasing	Hbl granulite	7a	3.10	49.24	8.48	13.08	10.26	11.01	0.31	2.37	0.71	1.43	0.48	0.26
SA1-4a	Kapuskasing	Granulite	8a	0.12	52.37	8.87	16.45	7.89	10.28	0.05	2.36	1.07	0.55	0.43	0.11

Note. Hbl: hornblende; Bt: biotite.

A third approach is to rely on *P–T* estimates of rocks with which the mafic granulites in question are interlayered, such as metapelitic rocks. This approach hinges, first, on the presence of such rocks (of the suites examined in this study, only the Namaqualand granulites allow this approach), second, that the two lithologies have experienced the same metamorphic conditions, and third, that these estimates are reliable.

A fourth approach involves the use of intersecting isolines of mineral modes on calculated phase diagrams, based on the measured modes and mineral compositions of the natural rocks (e.g. Powell & Holland, 2008). This approach assumes that the thermodynamically predicted phase diagrams and associated isolines are accurate, which to some degree contradicts the aim of this study which is to assess whether the predicted modes and mineral compositions provide a good match to the natural data. It is also difficult to apply in practice when there may be no mineral assemblage fields on the phase diagram that exactly match the observations, forcing decisions about which aspects of the mismatches are the more significant, and whether minerals of small modal abundance are significant.

A fifth approach, for rocks that show evidence for partial melting, involves assuming that the peak *P–T* conditions experienced by the rocks lies on the solidus specific to the rock composition. This method assumes that dehydration melting of hornblende, perhaps additionally biotite, was the operative process to produce the garnet and pyroxenes. For such rocks that contain combinations of pyroxene and garnet yet also contain the hydrous reactant phases hornblende and/or biotite, the implication is that the maximum *P–T* conditions the rocks experienced were within a reaction interval where the rocks had the capacity to produce more pyroxene and/or garnet and a melt phase if heated further. Thus, the *P–T* conditions would be represented by the solidus for the measured rock composition. In a practical sense, the *P–T* estimate for such rocks would be the point on the solidus closest to the observed modal mineralogy of the rock.

Even accepting the theoretical rationale for the solidus approach, the position of the solidus in the calculated phase diagrams is model-dependent, and so it suffers from some of the same limitations as the intersecting isolines approach. In addition, the solidus approach is not applicable to granulite facies rocks that were produced by processes other than dehydration melting. Alternative processes that can generate granulite facies mineral assemblages include infiltration by low a(H_2O) fluid (Janardhan, Newton, & Hansen, 1982; Newton, Smith, & Windley, 1980), or diffusion of H_2O down chemical potential gradients if the rocks in question are immediately adjacent to rocks of low a(H_2O) that can act as a sink for H_2O (Waters, 1988). This latter scenario applies to the mafic granulites from Namaqualand and therefore one of the other approaches is required.

Accepting that there is no universally applicable "best" method for estimating *P–T* conditions, we have adopted the intersecting isolines of mineral modes approach. To refine the *P–T* conditions of formation within the assemblage fields, isolines of equal modal proportions were calculated for the major phases. Using these as guidelines, the modal mineral proportions were determined at several points throughout the chosen assemblage field. The point where the mismatch between calculated and observed modes of major phases was the smallest was chosen as the initial estimate of the *P–T* conditions. In study areas where samples were collected in close proximity, such that the *P–T* conditions they experienced were likely the same, positions were adjusted slightly so that the samples had the same *P–T* estimates. The reliability of the resultant *P–T* estimate was assessed for each rock by consideration of one or several of the other approaches. For example, in Namaqualand, the modal isoline *P–T* estimate was matched with pelite thermobarometry, while at Kapuskasing, where the rocks are interpreted to have undergone dehydration melting of hornblende, the isoline *P–T* estimate was ensured to lie close to the solidus. These finalized points represent our reference *P–T* conditions for the formation of the observed assemblages (stars in Figures 3–8). In some cases, the *P–T* estimate for the preserved assemblage represents the conditions at which the rock equilibrated and will lie down-grade of actual peak *P–T*. However, this makes no difference to our analysis since we compare the preserved assemblage observed in the rock to an assemblage thermodynamically calculated at the approximated *P–T* conditions of preservation. An important point, which becomes clear later in the paper, is that the accuracy of the estimated *P–T* condition of each rock turns out not to be crucial to the degree of mismatch between predicted and observed mineral compositions.

4.5 | Mineral composition comparison

Compositions of phases within the modelled equilibrium assemblage were ascertained via examination of the readbulk-info matrix produced by THERMOCALC, which defines the proportions and compositions of all phases in the system in terms of oxide components. These results were used to calculate cation distributions/site allocations in amphibole and clinopyroxene and are compared to measured values in Tables 2 and 3, as well as in 1:1 plots (Figure 9a–d). Elements for which the number of observed cations is well predicted by the models will lie on the 1:1 line. The calcsdnle script in THERMOCALC was used, where possible,

to derive ±2σ values for the calculated number of each cation in amphibole and clinopyroxene; these are stated in Tables 2 and 3, and shown as error bars on 1:1 plots (Figure 9a–d), allowing comparison to the ±2σ values on measured cations derived from microprobe analyses.

Owing to the recognized issue of retrograde diffusional modification of compositions achieved at peak *P–T* conditions in granulite facies rocks (Frost & Chacko, 1989), and the fact that there is inherent uncertainty on the absolute position of phase assemblage field boundaries in *P–T* space (Powell & Holland, 2008), calculated amphibole and clinopyroxene compositions were examined over a range of *P–T* conditions, ±1 kbar and ±50°C, centred on the reference conditions (coloured squares and stars in Figures 3–8). Calculating an "uncertainty box" allows examination of the extent of compositional change away from the reference point. Comparisons of the calculated and observed values are portrayed graphically in Figures 10 and 11; shaded ellipses display the spread of calculated values, with each sample's ellipse colour coded to match the "uncertainty box" of the corresponding phase diagram, while cross-hatched ellipses exhibit the spread of observed values.

5 | PHASE EQUILIBRIUM MODELLING RESULTS

5.1 | Assemblage fields

In general, the assemblage fields and phase boundaries for all the studied samples resemble those shown by Palin, White, et al. (2016) for upper amphibolite- and granulite facies rocks of MORB-like composition. It was possible to locate a stability field containing an exact match to the observed assemblage for two of the samples studied here (DWN-346 and SA1-4a; Figures 3a and 8a respectively). In three cases, minor minerals were predicted that were not observed in the rock, including biotite in DWN-362, ilmenite in 87-G-3B and K-feldspar in SA1-13. For S98-15, the calculated stability field for the observed assemblage occurs at unrealistic *P–T* conditions and modal abundance estimates for major phases in this *P–T* range were disproportionate; therefore, a calculated assemblage was instead chosen that left out an observed minor mineral (biotite). However, even in these last four samples, only a single phase is either included or excluded, and the minor phase in question represents less than 2.0% of the mode; this can

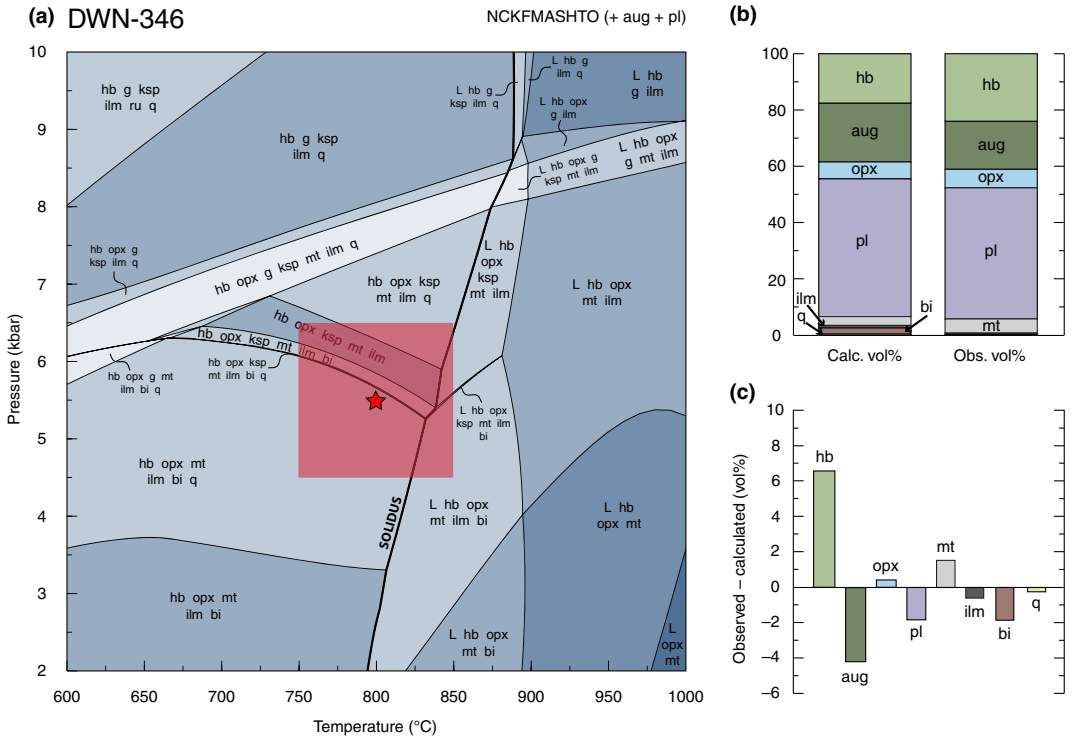

FIGURE 3 (a) Calculated *P–T* phase diagram for sample DWN-346. The star indicates the reference *P–T* conditions based on the observed mineral assemblage, while the square marks an area ±1 kbar and ±50°C around this point. (b) Comparison of calculated (left) versus observed (right) phase proportions (vol.%). Proportions shown here were calculated at 5.5 kbar, 800°C represented by the star in part (a). (c) Up–down bar chart showing the absolute difference between calculated and observed phase proportions. Positive differences indicate that the phase was more abundant in the sample than calculated via phase diagram modelling; negative differences indicate the opposite

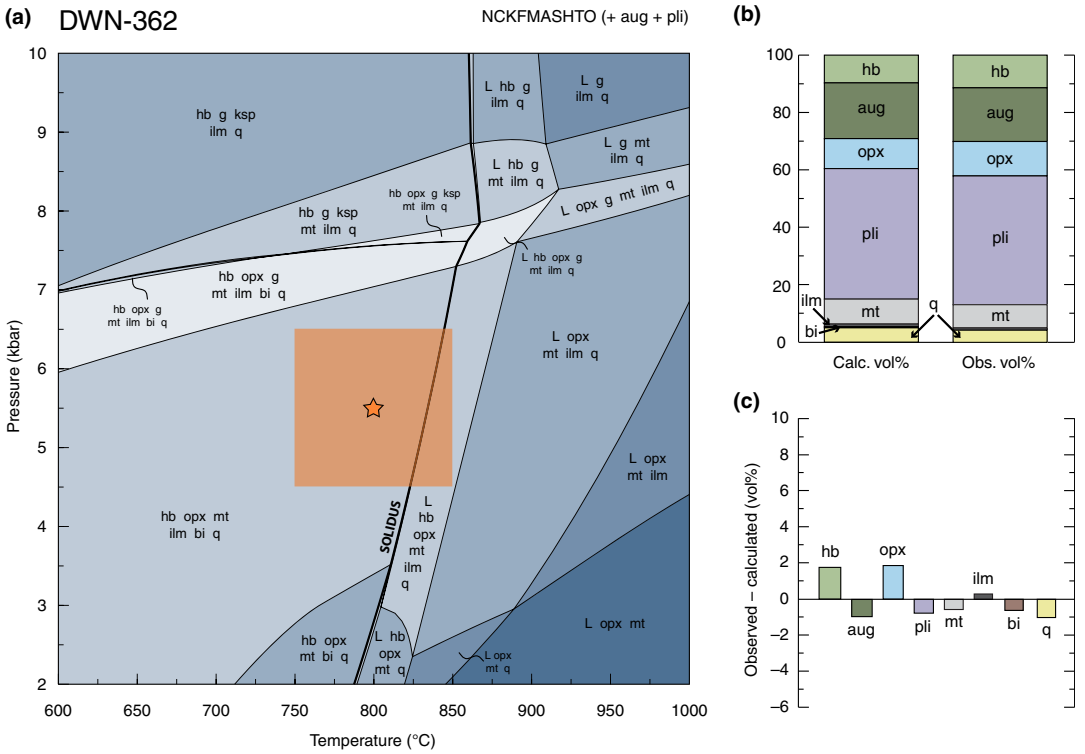

FIGURE 4 As for Figure 3, but for sample DWN-362. (a) Calculated *P–T* phase diagram, reference *P–T* conditions (star: 5.5 kbar, 800°C) and associated uncertainty box. (b) Phase proportion comparison. (c) Absolute differences in volume proportions

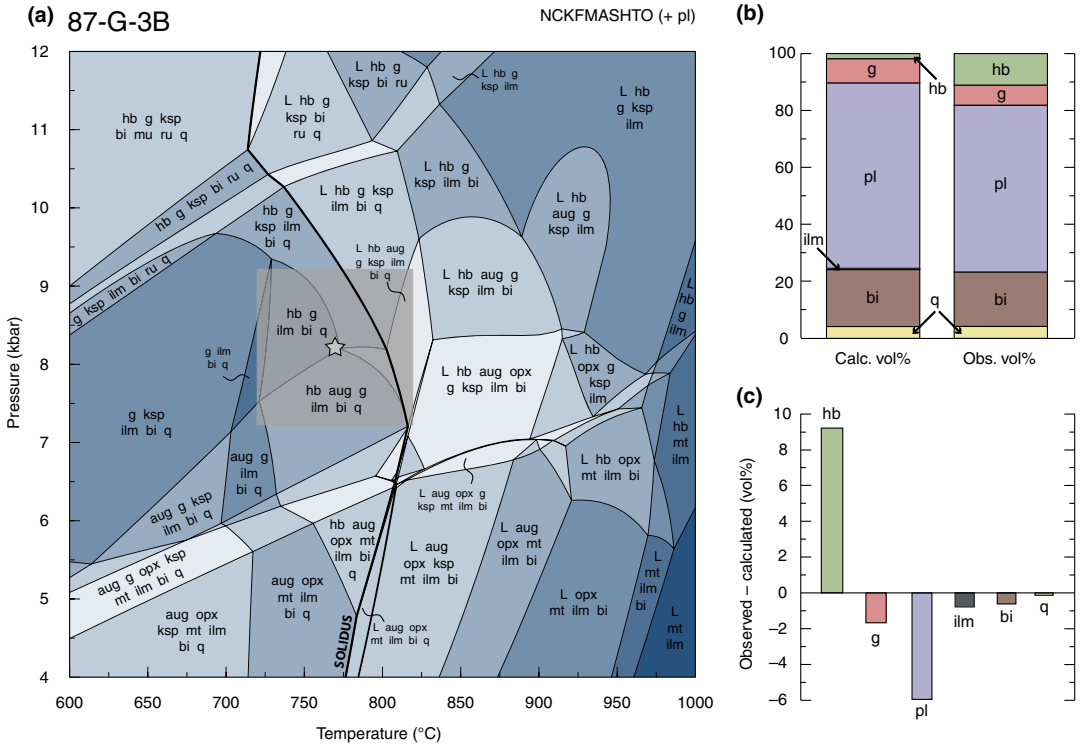

FIGURE 5 As for Figure 3, but for sample 87-G-3B. (a) Calculated *P–T* phase diagram, reference *P–T* conditions (star: 8.2 kbar, 770°C) and associated uncertainty box. (b) Phase proportion comparison. (c) Absolute differences in volume proportions

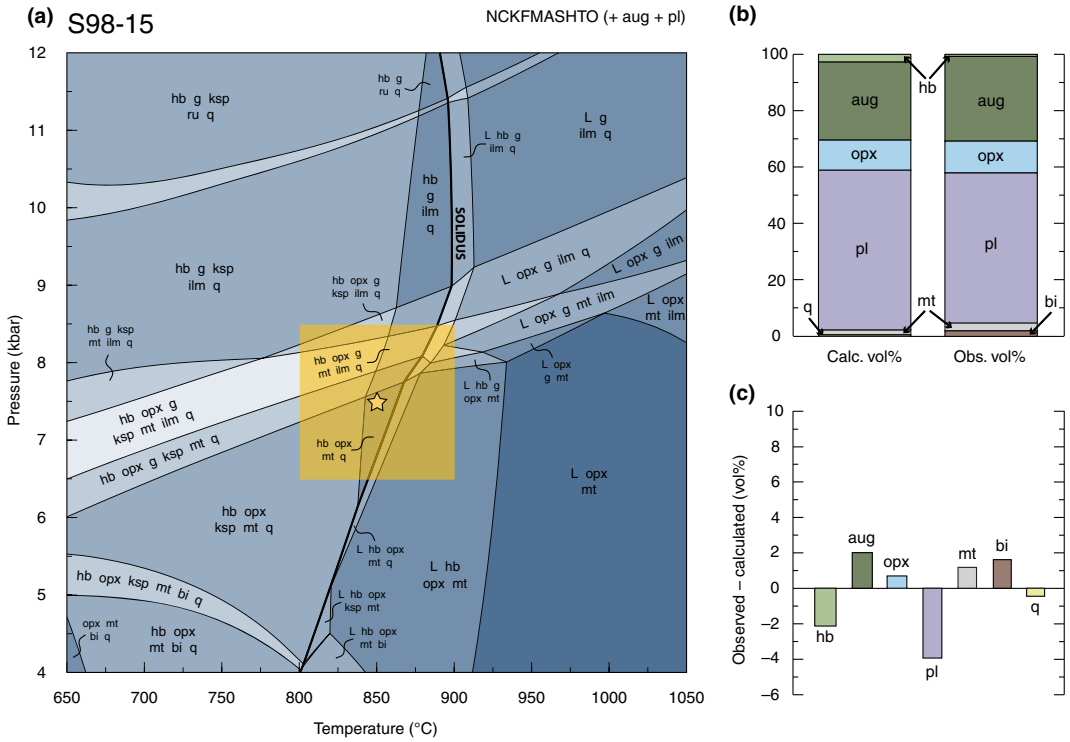

FIGURE 6 As for Figure 3, but for sample S98-15. (a) Calculated *P–T* phase diagram, reference *P–T* conditions (star: 7.5 kbar, 850°C) and associated uncertainty box. (b) Phase proportion comparison. (c) Absolute differences in volume proportions

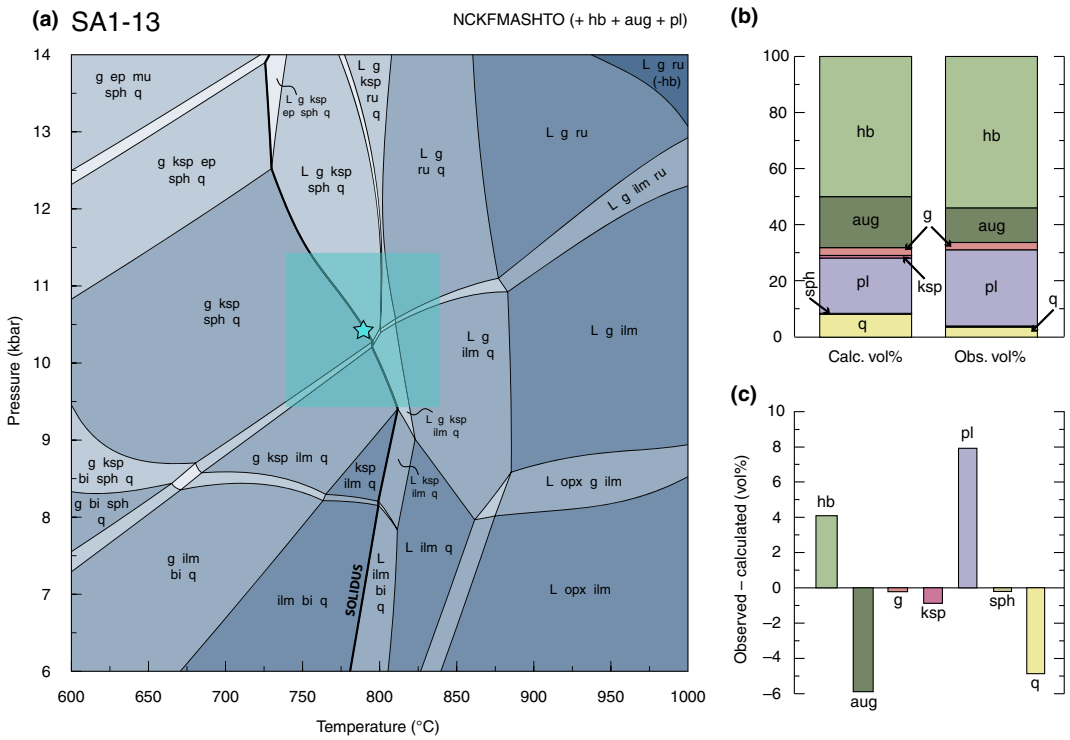

FIGURE 7 As for Figure 3, but for sample SA1-13. (a) Calculated *P–T* phase diagram, reference *P–T* conditions (star: 10.4 kbar, 795°C) and associated uncertainty box. (b) Phase proportion comparison. (c) Absolute differences in volume proportions

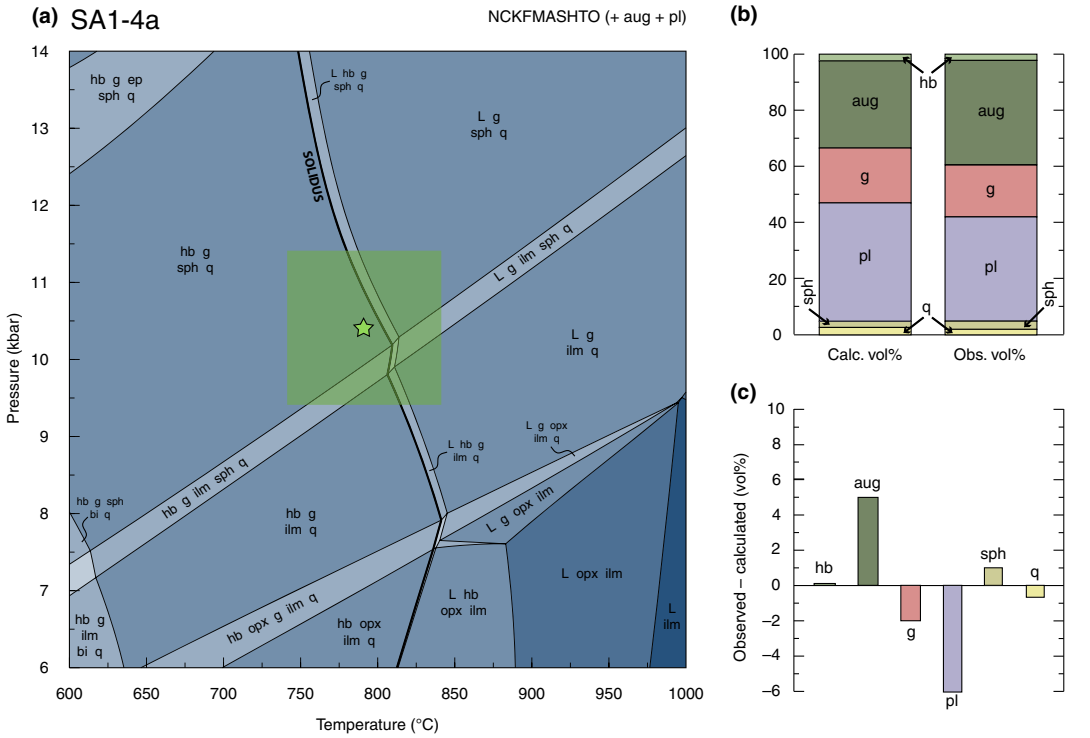

FIGURE 8 As for Figure 3, but for sample SA1-4a. (a) Calculated *P–T* phase diagram, reference *P–T* conditions (star: 10.4 kbar, 795°C) and associated uncertainty box. (b) Phase proportion comparison. (c) Absolute differences in volume proportions

be accounted for by uncertainty on the bulk composition, as shown in the Section 5.3.

5.2 | Reference *P–T* conditions

Following the approach defined above, estimates for the *P–T* of formation were determined by minimising the difference between calculated and observed modes of major minerals. In Namaqualand, calculated and observed phase proportions have minimal mismatch at 5.5 kbar and 800°C for DWN-346 and DWN-362 (stars in Figures 3a and 4a). For Cone Peak, an estimate of 8.2 kbar and 770°C was determined (grey star, Figure 5a). In the Lewisian Complex, reference *P–T* conditions of 7.5 kbar and 850°C were selected (yellow star, Figure 6a), because these gave the best match with previous phase equilibrium modelling studies (Feisel et al., 2018; Johnson & White, 2011). For the two Kapuskasing samples, collected in close proximity, the minimal mismatch was located close to the solidus, at 10.4 kbar and 795°C (stars in Figures 7a and 8a).

5.3 | Mineral modes

The best match between calculated and observed modes occurred in sample DWN-362, where differences were less than 2.0% (Figure 4b,c). S98-15 exhibited the next best fit with only plagioclase showing a >2.0% difference (Figure 6b,c). However, in DWN-346, 87-G-3B, SA1-13, and SA1-4a, significant mismatches exist for hornblende, augite, and plagioclase (Figures 3, 5, 7, and 8). By examining the relative sense of the mismatches, it was determined that in the most hornblende-rich rocks, DWN-346, DWN-362, 87-G-3B, and SA1-13, the proportion of hornblende is significantly underestimated (1.7–9.2% mismatch) and the proportion of augite overestimated (0.9–5.9% mismatch). In contrast, the match between predicted and observed hornblende and augite modes is better in the two hornblende-poor samples (S98-15 and SA1-4a). No persistent under- or overprediction of the modal amount of garnet, accessory oxides, quartz, or plagioclase was found.

The calcsdnle script in THERMOCALC was used to determine if the uncertainty on the calculated modal proportions could account for the discrepancies described between calculated and observed hornblende, augite, and plagioclase modes. The relative percentage uncertainty on the calculated phase volumes (Figure 12a) was propagated through calculations to find the absolute percentage uncertainty on the calculated phase volume. Figure 12b compares this absolute percentage uncertainty to the actual difference found between calculated and observed values, showing that although small differences in proportions can be accounted for by this uncertainty, larger differences cannot be.

TABLE 2 Mean observed (Obs) and calculated (Calc) amphibole cation compositions (23-oxygen+Ti cations/2 formula unit), for all six samples. The spread in the number of cations for the observed and calculated populations is expressed as 2 SDs; however, it was only possible to calculate the observed spread for analyses collected as part of this study, not those taken from the literature (e.g. SA1-13 and SA1-4a)

	DWN-346		DWN-362		87-G-3B		S98-15		SA1-13		SA1-4a	
	Obs	Calc	Obs	Calc	Obs	Calc	Obs	Calc	Obs	Calc	Obs	Calc
Si	6.55 ± 0.06	6.07 ± 0.29	6.53 ± 0.12	6.19 ± 0.28	6.28 ± 0.11	5.94 ± 0.29	6.13 ± 0.09	5.93 ± 0.31	6.33	5.84 ± 0.27	6.28	5.98 ± 0.21
Al	1.87 ± 0.08	2.48 ± 0.32	1.81 ± 0.12	2.41 ± 0.31	2.12 ± 0.10	2.82 ± 0.33	2.44 ± 0.15	2.70 ± 0.34	2.10	3.02 ± 0.31	2.28	3.04 ± 0.26
Al(iv)	1.45 ± 0.06	1.93 ± 0.29	1.47 ± 0.12	1.81 ± 0.28	1.72 ± 0.11	2.06 ± 0.29	1.87 ± 0.09	2.07 ± 0.31	1.67	2.16 ± 0.27	1.72	2.02 ± 0.21
Al(vi)	0.42 ± 0.07	0.55 ± 0.12	0.34 ± 0.05	0.59 ± 0.14	0.40 ± 0.07	0.75 ± 0.16	0.57 ± 0.08	0.63 ± 0.14	0.43	0.86 ± 0.15	0.56	1.01 ± 0.15
Ti	0.23 ± 0.02	0.14 ± 0.03	0.14 ± 0.01	0.12 ± 0.02	0.30 ± 0.05	0.16 ± 0.02	0.23 ± 0.07	0.12 ± 0.07	0.19	0.17 ± 0.03	0.19	0.18 ± 0.03
Fe^{3+}	0.35 ± 0.09	0.70 ± 0.22	0.65 ± 0.10	0.64 ± 0.22	0.53 ± 0.12	0.59 ± 0.20	0.42 ± 0.15	0.71 ± 0.21	0.68	0.53 ± 0.14	0.55	0.27 ± 0.13
Fe^{2+}	1.18 ± 0.10	1.16 ± 0.10	0.93 ± 0.11	1.18 ± 0.10	2.15 ± 0.08	1.97 ± 0.15	1.51 ± 0.14	1.29 ± 0.12	1.64	1.53 ± 0.10	1.88	1.57 ± 0.10
Mg	2.78 ± 0.09	2.82 ± 0.23	2.90 ± 0.12	2.87 ± 0.25	1.62 ± 0.07	1.82 ± 0.14	2.23 ± 0.09	2.70 ± 0.25	2.04	2.09 ± 0.14	1.80	2.17 ± 0.14
Ca	1.90 ± 0.05	1.59 ± 0.20	1.88 ± 0.03	1.59 ± 0.24	1.83 ± 0.06	1.60 ± 0.14	1.91 ± 0.05	1.49 ± 0.26	1.89	1.69 ± 0.11	1.90	1.69 ± 0.11
Na	0.37 ± 0.05	0.52 ± 0.07	0.35 ± 0.04	0.32 ± 0.05	0.41 ± 0.08	0.67 ± 0.08	0.35 ± 0.04	0.56 ± 0.09	0.45	0.73 ± 0.10	0.42	0.75 ± 0.06
Na(M4)	0.13 ± 0.03	0.04 ± 0.02	0.15 ± 0.02	0.01 ± 0.01	0.17 ± 0.03	0.10 ± 0.05	0.12 ± 0.03	0.05 ± 0.02	0.13	0.12 ± 0.06	0.12	0.11 ± 0.05
Na(A)	0.24 ± 0.04	0.48 ± 0.07	0.37 ± 0.03	0.34 ± 0.05	0.25 ± 0.07	0.56 ± 0.06	0.23 ± 0.05	0.51 ± 0.09	0.32	0.60 ± 0.08	0.30	0.63 ± 0.03
K	0.29 ± 0.02	0.12 ± 0.07	0.22 ± 0.03	0.17 ± 0.05	0.36 ± 0.03	0.11 ± 0.06	0.49 ± 0.08	0.14 ± 0.09	0.15	0.11 ± 0.08	0.21	0.04 ± 0.03
X_{Mg}	0.70 ± 0.03	0.71 ± 0.02	0.76 ± 0.03	0.71 ± 0.02	0.43 ± 0.01	0.48 ± 0.09	0.60 ± 0.03	0.68 ± 0.02	0.55	0.58 ± 0.01	0.49	0.58 ± 0.05

TABLE 3 Mean observed (Obs) and calculated (Calc) clinopyroxene cation compositions (6-oxygen formula unit), for the five augite-bearing samples. The spread in the number of cations for the observed and calculated population is expressed as 2 *SD*s; however, it was only possible to calculate the observed spread for analyses collected as part of this study, not those taken from the literature (e.g. SA1-13 and SA1-4a). The uncertainty on calculated cations is only stated when it was possible to derive the value from the compositional parameters THERMOCALC provides

	DWN-346		DWN-362		S98-15		SA1-13		SA1-4a	
	Obs	Calc	Obs	Calc	Obs	Calc	Obs	Calc	Obs	Calc
Si	1.96 ± 0.02	1.86 ± 0.15	1.94 ± 0.02	1.78 ± 0.18	1.93 ± 0.03	1.80 ± 0.16	1.94	1.89 ± 0.11	1.94	1.97 ± 0.03
Al	0.09 ± 0.01	0.16	0.09 ± 0.02	0.25	0.15 ± 0.04	0.23	0.10	0.15	0.12	0.07
Fe^{3+}	0.02 ± 0.03	0.15 ± 0.13	0.04 ± 0.04	0.20 ± 0.17	0.04 ± 0.03	0.20 ± 0.15	0.06	0.15 ± 0.08	0.04	0.06 ± 0.02
Fe^{2+}	0.22 ± 0.04	0.28	0.25 ± 0.06	0.29	0.27 ± 0.04	0.31	0.31	0.37	0.37	0.37
Mg	0.76 ± 0.02	0.63	0.75 ± 0.03	0.56	0.67 ± 0.03	0.55	0.65	0.49	0.61	0.59
Ca	0.91 ± 0.04	0.89 ± 0.04	0.89 ± 0.06	0.92 ± 0.02	0.90 ± 0.04	0.88 ± 0.03	0.88	0.89 ± 0.04	0.88	0.87 ± 0.03
Na	0.03 ± 0.00	0.03 ± 0.02	0.02 ± 0.00	0.01 ± 0.00	0.04 ± 0.01	0.03 ± 0.02	0.05	0.07 ± 0.05	0.05	0.07 ± 0.03
X_{Mg}	0.77 ± 0.03	0.69 ± 0.04	0.75 ± 0.05	0.66 ± 0.04	0.72 ± 0.03	0.64 ± 0.03	0.68	0.57 ± 0.05	0.62	0.62 ± 0.02

As bulk composition is the primary control on phase diagram topology and phase proportions/compositions in an equilibrium assemblage (e.g. Stüwe & Powell, 1995) it must be considered whether the mismatches alluded to above are still significant when uncertainty on the bulk compositions is accounted for. The sensitivity of the chosen bulk compositions for modelling was tested using a Monte Carlo-type randomization that incorporated a ±5% (relative) uncertainty on each oxide value. For each sample, 20 new bulk compositions were produced and then the corresponding phase proportions calculated at the same reference *P–T* conditions as the original calculations. These phase proportions are plotted on box and whisker diagrams (Figure 13), where the upper and lower limits of each box are the 75th and 25th percentiles, respectively, the 50th percentile is the line within the box, and the whiskers represent the 5th and 95th percentiles. Figure 13 shows that even considering this large uncertainty (±5% on each oxide value) on the bulk composition, the same trends emerge with the most hornblende-rich rocks exhibiting underestimated hornblende and overestimated augite.

5.4 | Mineral compositions

In the analysis that follows, emphasis is placed on the compositions of amphibole and clinopyroxene because these are the minerals for which the new *a–x* relations of Green et al. (2016) were developed. Mismatches were generally smaller for the other minerals (Tables 2 and 3), with the exception of garnet in which Al and Ca are underestimated and Fe^{3+} is overestimated. Comparisons of the calculated and observed compositions of clinopyroxene and hornblende at the reference *P–T* conditions are shown in Figure 9 and Tables 2 and 3. These comparisons were then extended across the respective uncertainty boxes in Figures 3a, 4a, 5a, 6a, 7a, and 8a, with no significant changes in the observed differences emerging.

5.4.1 | Amphibole

Figure 9a illustrates tetrahedral site cations in amphibole, showing how the modelled compositions underestimate Si and consequently overestimate Al, Al(iv), and Al(vi). This Al/Si discrepancy is also exhibited by the mismatch of tschermakite content ($Al_4Mg_{-2}Si_{-2}$), and represents the most prominent difference in hornblende, since there is no overlap on Figure 10a or b between calculated and observed compositions, even when including the uncertainty on the *P–T* estimate. As argued in the earlier discussion regarding formula recalculation (Section 2.3), Fe^{3+} recalculation and the amount of deprotonation do not appear to be significant factors for the comparison; therefore, the Al/Si mismatch indicates an overestimation of tschermak-type substitutions.

The Ca content is underpredicted in all six samples by 0.2–0.5 cations (Figure 9c), with once again no overlap found when comparing values calculated over the uncertainty box to the range of those observed (Figure 10c). Since Na(M4) is also underestimated by the models (Figure 9c), this places a much greater amount of Mg and Fe^{2+} on the M4 site (cummingtonite/grunerite component), than is found in natural, high-*T* hornblendes, in turn causing the aforementioned deficit in amphibole's Ca content.

With the exception of DWN-362, predicted values for Na in the A-site are overestimated by up to 0.3 cations and for K, underestimated by up to 0.4 cations (Figure 9c); these represent large discrepancies when only 0.2–0.6 total cations of either Na or K are observed on the A-site of natural amphibole (Figure 10d). This low K_2O has consequences for how the bulk K_2O budget is distributed between other calculated phases.

In four of the six samples, predicted Fe^{2+} and Mg contents are under- and overpredicted respectively (Figure 9b);

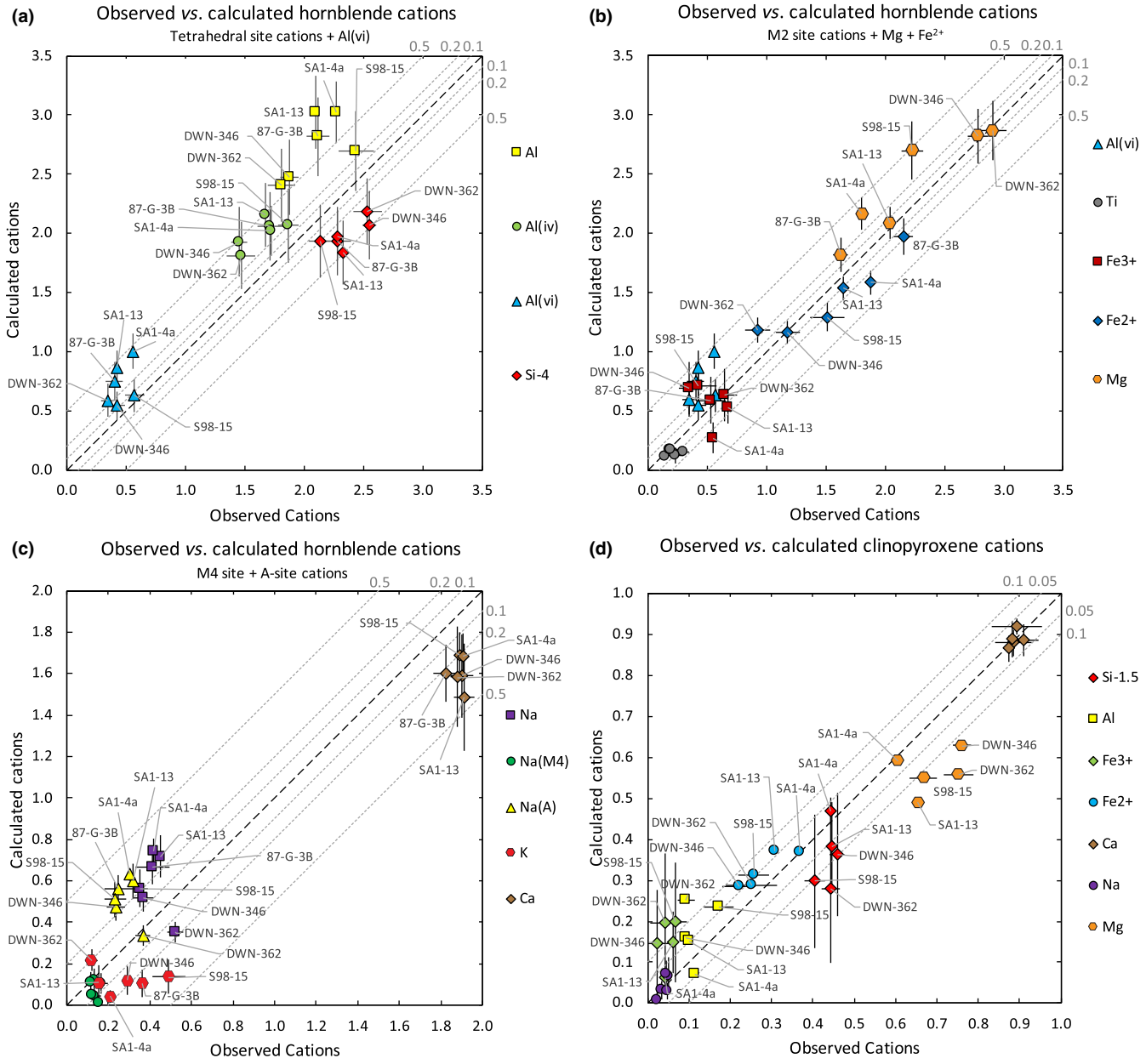

FIGURE 9 Comparison of calculated and observed (a–c) amphibole and (d) clinopyroxene compositions. (a) Amphibole tetrahedral site cations (Si and Al(iv)) along with total Al and Al(vi). (b) Amphibole M2 site cations (Al(iv), Ti and Fe^{3+}), as well as Fe^{2+} and Mg, which may substitute into any M site. (c) Amphibole M4 site (Ca and Na(M4)) and A-site cations (K and Na(A)). (d) Clinopyroxene cations (Si, Al, Fe^{2+}, Fe^{3+}, Mg, Ca, and Na). Note that the number of calculated and observed Si cations has been reduced by 4 and 1.5 for amphibole and clinopyroxene, respectively, due to the relatively large number. Each point represents that elements value in one sample, labelled where possible, meaning there are six values for each element for (a–c) amphibole and five for each element for (d) clinopyroxene. Those elements for which the number of observed cations is well predicted by the models will lie on the 1:1 line. 2σ uncertainties are plotted as error bars where available. Grey dotted lines show cation differences between calculated and observed values

this results in predicted X_{Mg} ratios that are too high (~0.05–0.10) in all but the two Mg-rich Namaqualand specimens (Figure 10c). Calculated versus observed Fe^{3+} contents are scattered (Figure 9b), which may be expected from the uncertainty of recalculation in natural hornblende analyses, but there is no obvious bias to higher or lower values. The Ti content is adequately predicted.

5.4.2 | Clinopyroxene

Concerning clinopyroxene, the most significant difference between predicted and calculated compositions concerns Fe^{2+} and Mg. Calculated Fe^{2+} contents were consistently higher than observed values by ~0.05 cations, and were accompanied by a commensurate or even larger deficiency

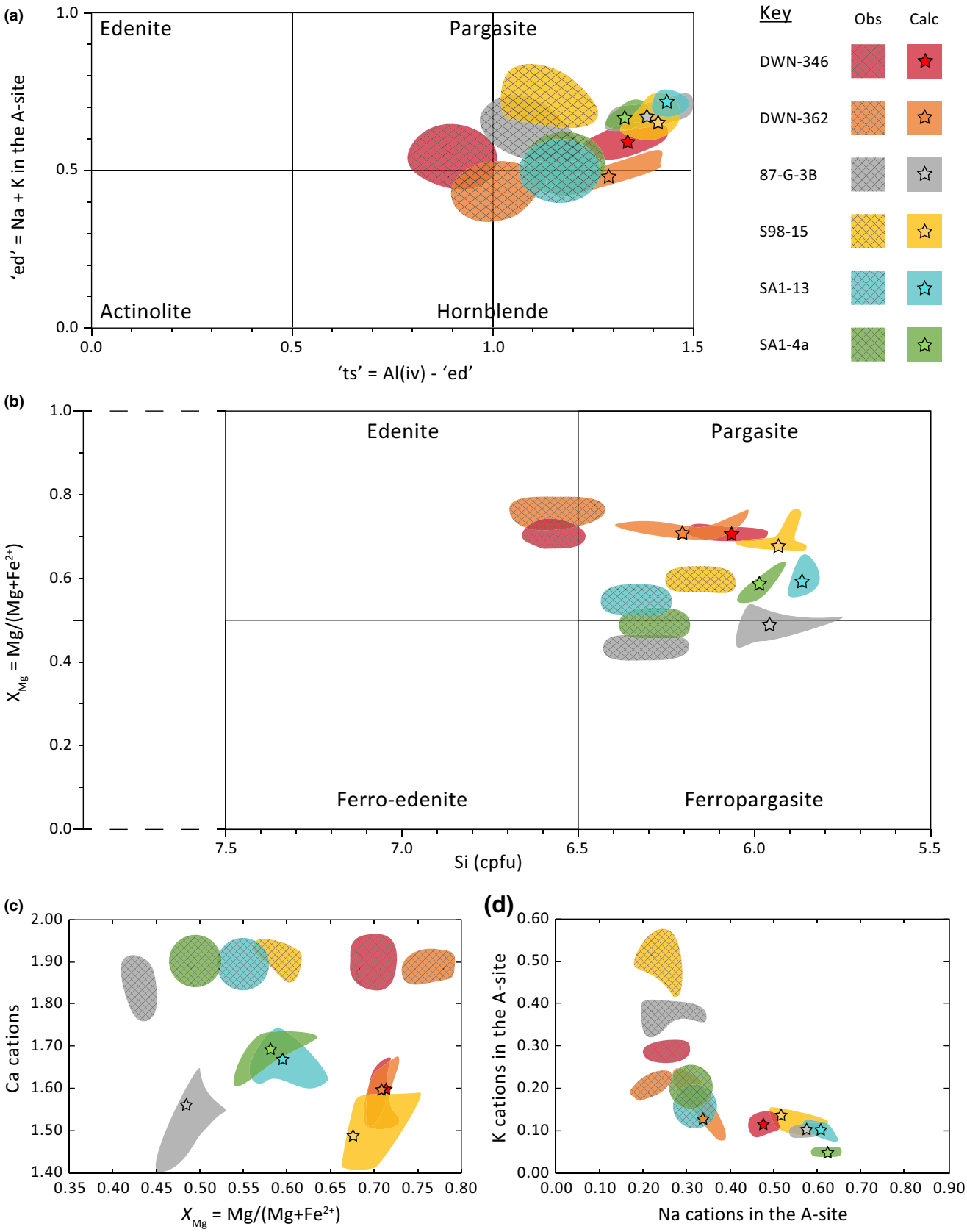

in Mg (Figure 9d). This mismatch is manifested in the calculated X_{Mg} ratio which is significantly lower (~0.05–0.10) than that for natural clinopyroxenes in four of the five samples (Figure 11a). Figure 14 depicts plotting positions of hornblende, garnet, orthopyroxene, and clinopyroxene in a CFM diagram; it shows that the predicted Fe–Mg

FIGURE 10 A comparison of calculated and observed compositions for the samples studied, each denoted by a colour according to the key. Cross-hatched ellipses represent the spread of measured compositions (the spread was estimated for those from the Kapuskasing), while stars and shaded ellipses represent reference *P–T* condition compositions and compositions calculated over a grid extending ±1 kbar and ±50°C respectively. The origin of these calculated compositions is explicated by comparison with Figures 3–8. Amphibole compositions are shown in terms of (a) the exchange vector edenite ("ed" = Na+K in A-site) and exchange vector tschermakite (ts: $Al_2Mg_{-1}Si_{-1}$), as in fig. 6 of Schumacher (2007); (b) the X_{Mg} ratio versus the total number of Si cations, as in fig. 3 of Leake et al. (1997); (c) the total number of Ca cations versus the X_{Mg} ratio; (d) the number of K cations in the A-site versus the number of Na cations in the A-site

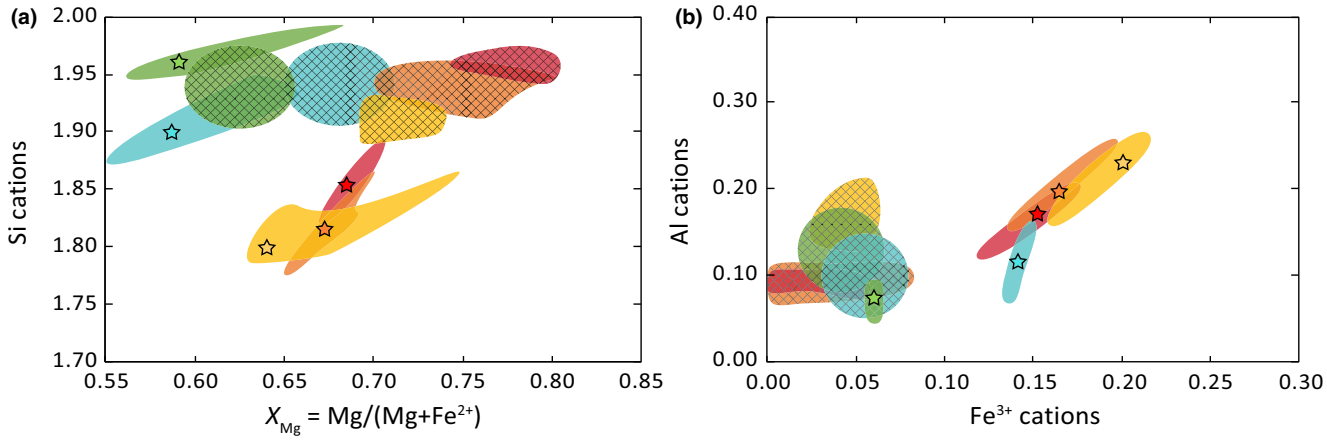

FIGURE 11 As for Figure 10, but for clinopyroxene compositions expressed in terms of (a) the total number of Si cations versus the X_{Mg} ratio; (b) the total number of Al cations versus the total number of Fe^{3+} cations

partitioning between amphibole and clinopyroxene (X_{Mg} in hb > aug) is the reverse of widely established patterns in natural rocks in which clinopyroxene is more magnesian than coexisting amphibole (cf. Hartel & Pattison, 1996; Huang et al., 2018; Kumar & Chacko, 1994; Loock, Stosch, & Seck, 1990; Pattison, 1991; Zhao, Wilde, Cawood, & Liu, 2000). This discrepancy pertains whether Fe^{3+} is included or not. A consequence is that the magnitude of predicted Fe–Mg partitioning between clinopyroxene and garnet, and between clinopyroxene and orthopyroxene, is smaller than observed. As discussed in Section 4.4, postpeak Fe–Mg exchange may have affected mineral compositions but correcting for this effect does not reverse the observed Fe–Mg partitioning between hornblende and clinopyroxene.

The number of Si and Al cations is typically underestimated (~0.05–0.15) and overpredicted (~0.10–0.15), respectively, with SA1-4a presenting an exception where the opposite occurs (Figures 9d and 11a,b); this indicates that the augite *a–x* relation, like that for amphibole, typically overestimates tschermak-type substitutions. The number of Fe^{3+} cations is overestimated in all cases, being significantly higher (~0.10–0.20) in four out of five samples (Figure 9d); however, it should be noted that the uncertainty on Fe^{3+} content is much greater than any other cation. Trends in Figure 11b show a correlation between calculated Fe^{3+} and Al, suggesting that a ferri-tschermak substitution, which is sensitive to *P–T* conditions, is overestimated by the model. With regard to the M2 site, its occupancy (Ca and Na, plus a small amount of Fe^{2+} and Mg) appears to be matched within uncertainty (Figure 9d).

6 | DISCUSSION AND CONCLUSIONS

6.1 | Source of the discrepancies

6.1.1 | Incorrect partitioning of elements between phases

An assessment was made to determine if the consistent compositional mismatches identified in amphibole and clinopyroxene could be attributed to modal or compositional patterns in other phases. If this is the case, mismatches may be the result of incorrect partitioning of elements between the different *a–x* relations. Except for Ca, no distinct correlation could be found that links cation discrepancies to mismatches of opposite and equal magnitude in the compositions of coexisting phases. In samples 87-G-3B, SA1-13, and SA1-4a, predicted garnet has a greater grossular component than observed, which could account for the low-amphibole Ca contents; however, comparable compositional mismatches were found between predicted and observed hornblende in garnet-bearing and garnet-free rocks, meaning incorrectly predicted garnet compositions cannot account for the

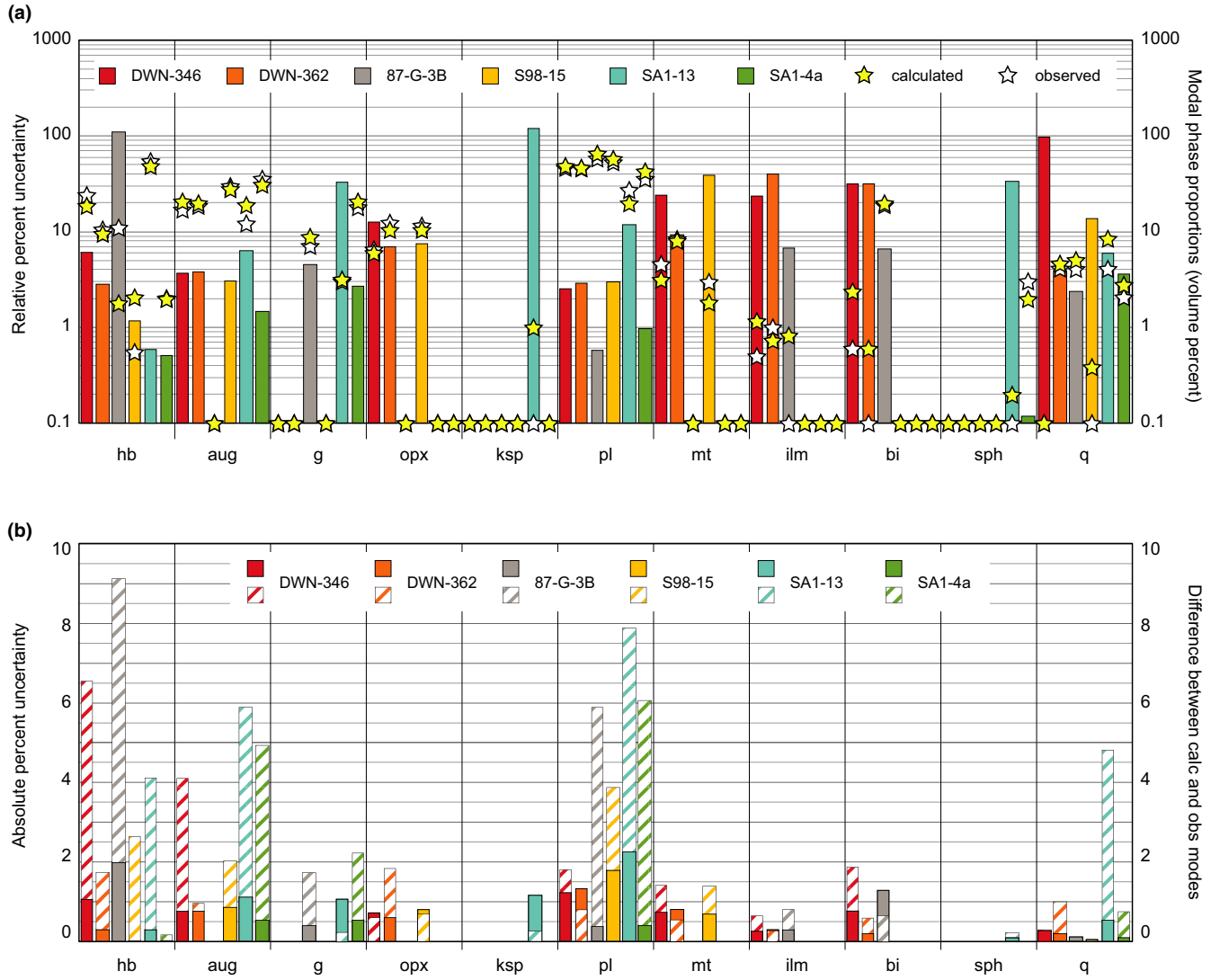

FIGURE 12 Plots produced using data from the calcsdnle script in THERMOCALC. (a) The relative percentage uncertainty on the calculated phase volume of each mineral (solid coloured bars), as well as the modal proportions observed and calculated (stars). (b) Propagated absolute percentage uncertainty on the calculated phase volume (solid coloured bars) and the actual difference between calculated and observed values (striped bars)

discrepancy. Therefore, amphibole's low Ca content is the result of overestimating the amount of Mg and Fe^{2+} on the M4 site.

These data imply that mismatches are due to the *a–x* relations for amphibole and clinopyroxene, and the way they interact. The largest Fe^{2+} and Mg discrepancies in hornblende and the smallest Fe^{2+} and Mg discrepancies in clinopyroxene occur for the hornblende poorest rocks; the reverse is true for hornblende-rich rocks. This correlation between the Fe^{2+} and Mg contents of the two phases is most clearly seen in Figure 9b,d; when calculated amphibole exhibits a deficit in Fe^{2+}, predicted clinopyroxene displays an enriched Fe^{2+} content, whereas the opposite is seen in Mg contents. The result is that K_D $(=(Fe^{2+}/Mg)_{aug}/(Fe^{2+}/Mg)_{hb})$ values for calculated compositions are always greater than those for observed compositions, and

FIGURE 13 Box and whisker plots for each sample depicting the volume per cent of calculated phase proportions at the reference *P–T* conditions for 20 different bulk compositions. These bulk compositions were determined using a Monte Carlo-type randomization that incorporates a ±5% (relative) uncertainty on each oxide value. The upper and lower limits of each box are the 75th and 25th percentiles, respectively, the 50th percentile is the line within the box, and the whiskers represent the 5th and 95th percentiles. White stars represent the observed modal percentage of each phase

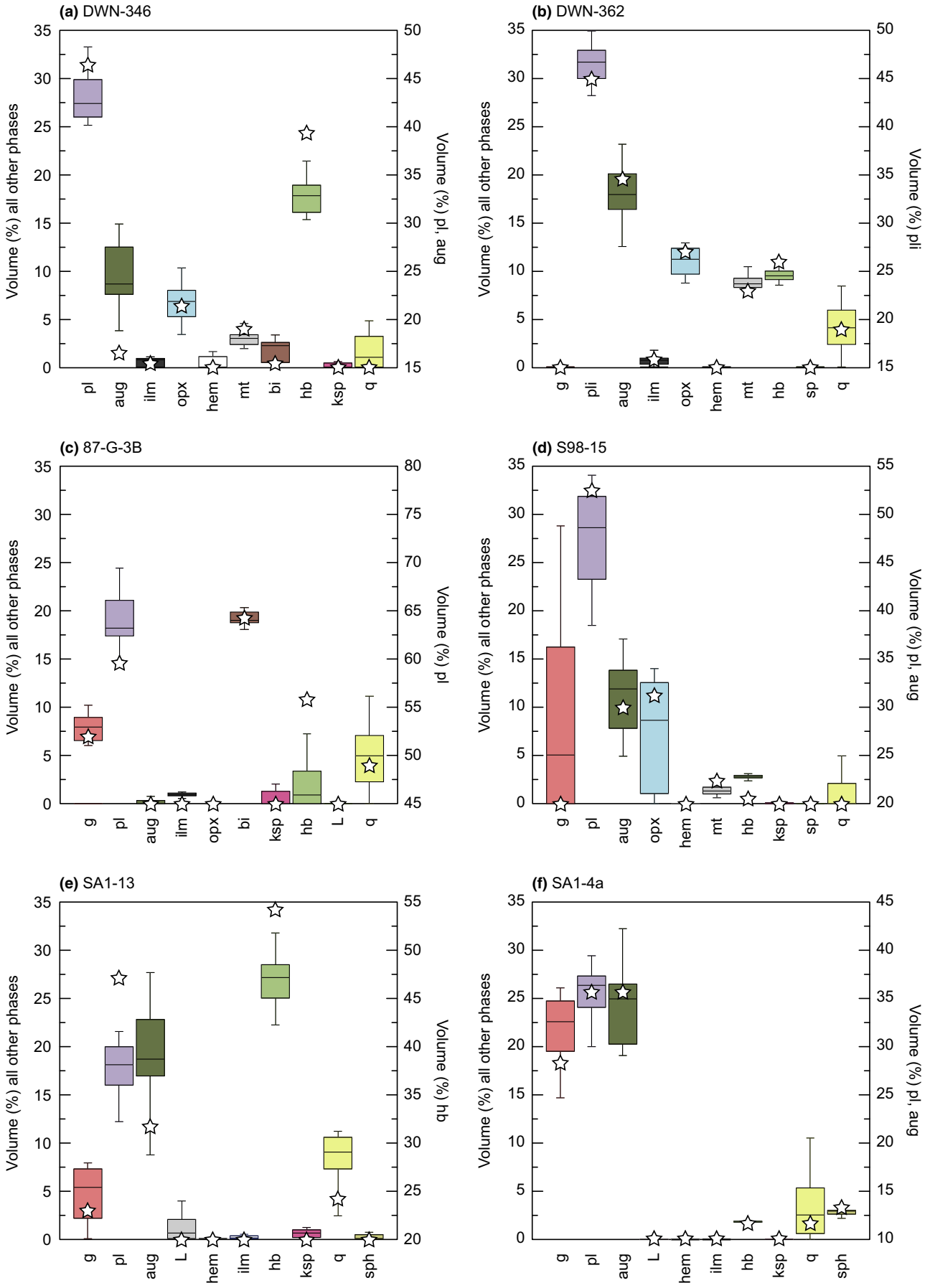
(a) DWN-346
Volume (%) all other phases
Volume (%) pl, aug
pl
aug
ilm
opx
hem
mt
bi
hb
ksp
q
(b) DWN-362
Volume (%) all other phases
Volume (%) pli
g
pli
aug
ilm
opx
hem
mt
hb
sp
q
(c) 87-G-3B
Volume (%) all other phases
Volume (%) pl
g
pl
aug
ilm
opx
bi
ksp
hb
L
q
(d) S98-15
Volume (%) all other phases
Volume (%) pl, aug
g
pl
aug
opx
hem
mt
hb
ksp
sp
q
(e) SA1-13
Volume (%) all other phases
Volume (%) hb
g
pl
aug
L
hem
ilm
hb
ksp
q
sph
(f) SA1-4a
Volume (%) all other phases
Volume (%) pl, aug
g
pl
aug
L
hem
ilm
hb
ksp
q
sph

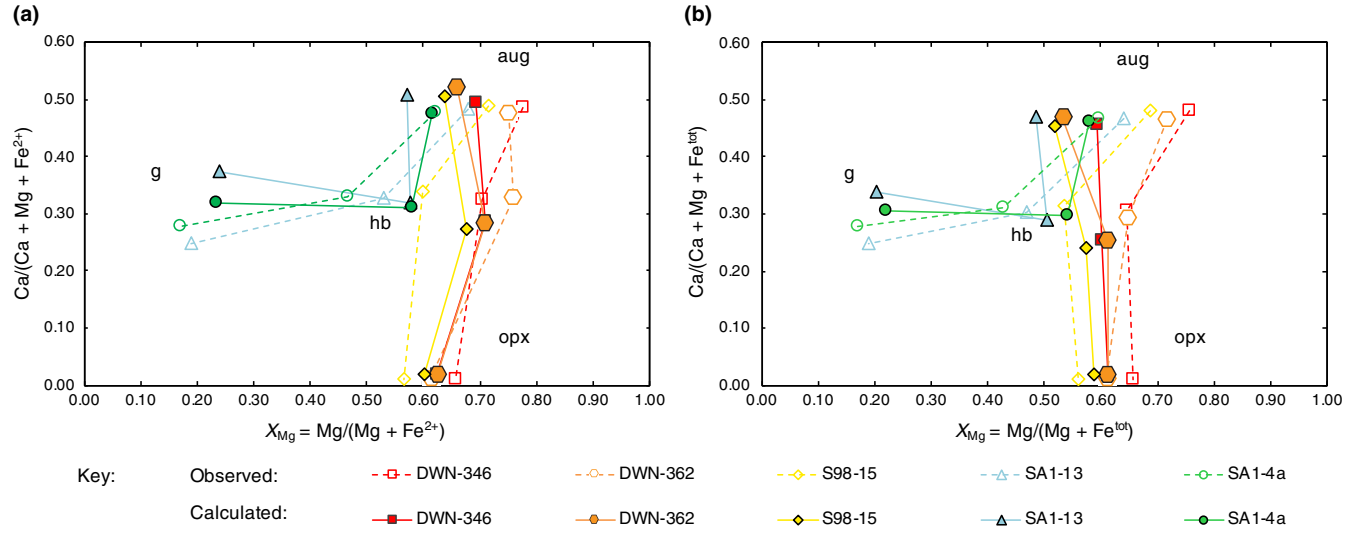

FIGURE 14 Diagrams plotting (a) Ca/(Ca+Mg+Fe^{2+}) against X_{Mg}=Mg/(Mg+Fe^{2+}) and (b) Ca/(Ca+Mg+Fe_{tot}) against X_{Mg}=Mg/(Mg+Fe_{tot}). For each sample, observed values for hornblende and clinopyroxene, as well as either garnet or orthopyroxene, are plotted as open symbols connected by dashed lines, whereas calculated values for these phases are shown as closed symbols connected by solid lines

in fact change from being less than 1.0 (observed) to greater than 1.0 (calculated), implying a reversal in partitioning of Fe^{2+} and Mg between the two minerals. This point is further illustrated in Figure 14, where the X_{Mg} ratio of amphibole is greater than that for clinopyroxene in four of the five samples. These discrepancies in Fe^{2+}/Mg contents result from the manner in which Fe^{2+} and Mg are partitioned between amphibole and clinopyroxene. Future clinopyroxene and amphibole *a–x* relations would ideally bring modelled Fe–Mg partitioning into agreement with the natural record, by using analyses for which Mössbauer or wet chemical data on Fe^{3+}/Fe^{2+} ratios are available.

Concerning Na and K, less of a systematic pattern exists in these natural samples when compared to Fe^{2+} and Mg. However, it appears that the new *a–x* relations cannot assign a sufficient number of K cations into amphibole. An

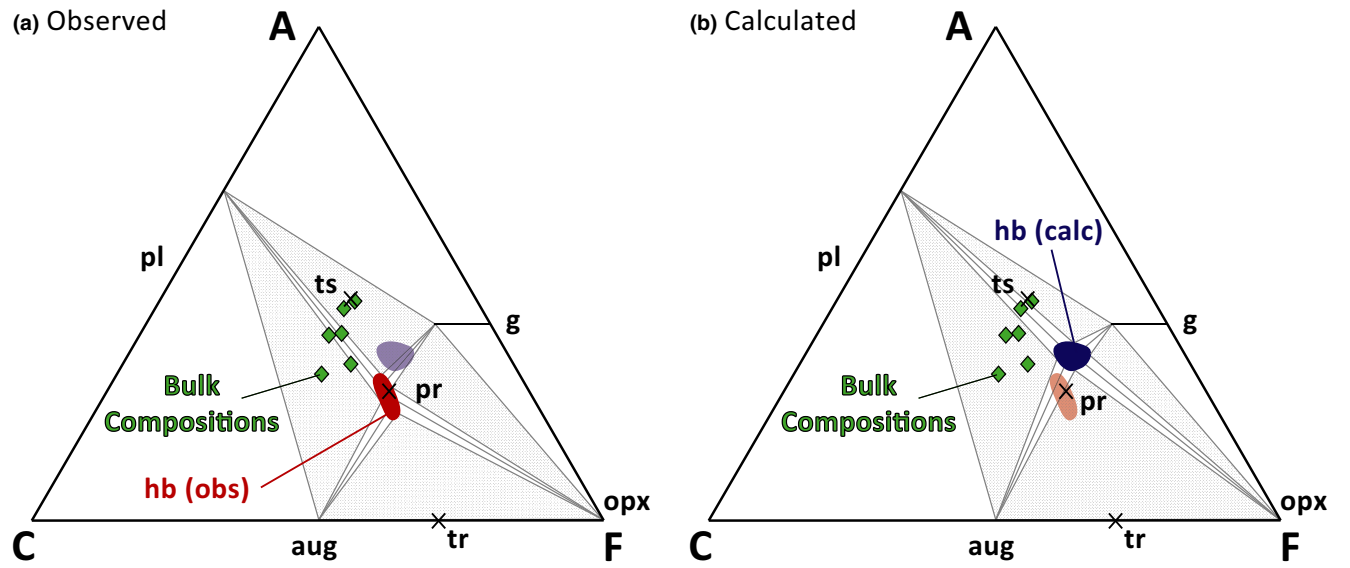

FIGURE 15 ACF diagrams created using (a) average compositions of observed hornblende in the six samples to produce the red ellipse and (b) hornblende compositions calculated at reference *P–T* conditions for the six samples to obtain the blue ellipse. End-member values were used for plagioclase, garnet, augite, and orthopyroxene to draw tie lines, while end-member amphibole compositions (ts = tschermakite, pr = pargasite and tr = tremolite) are shown for comparison purposes. Bulk compositions for each of the samples, listed in Table 1, are plotted as green diamonds. ACF proportions were determined in the same manner as Eskola (1920) but to expand the range of Al contents, the A component (Al_2O_3+Fe_2O_3−Na_2O−K_2O) was halved, similar to the method of Spear (1993)

improved partition coefficient for the K-pargasite end-member may be obtained by recalibration with reference to natural biotite- or K-feldspar-bearing high-*T* assemblages.

6.1.2 | Incorrect prediction of major substitution vectors

A pattern that emerges from the analysis of calculated compositions of both amphibole and clinopyroxene is the overestimation of tschermak-type substitutions by the *a–x* relations, manifested by predicted Al/Si ratios in both minerals that are too high. To our knowledge, earlier versions of amphibole *a–x* relations (e.g. Diener & Powell, 2012; Diener, Powell, White, & Holland, 2007) used in conjunction with thermodynamic data set ds55 (Holland & Powell, 1998) did not result in as marked mismatches between the predicted and observed Al/Si ratio. In hornblende, this is not linked to a discrepancy in Ti or Fe^{3+} content, or of systematic error in the extent of deprotonation substitution, but appears to be a direct overestimation of the charge-balanced Al(vi)Al(iv) for MgSi tschermak substitution, implying that the thermodynamic model overstabilizes Al-rich hornblende.

In hornblende, underestimation of Ca in the model seems to be associated with the overestimation of the Mg and Fe^{2+} content of the M4 site, linked to the overstabilization of the cummingtonite and grunerite end-members. This is likely due to these aspects of the calibration having been done to match lower temperature natural assemblages (Dale, Powell, White, Elmer, & Holland, 2005; Diener et al., 2007). Insofar as these M4 site substitutions are analogous to the Mg and Fe^{2+} contents of the M2 site in clinopyroxene (i.e., of enstatite-ferrosilite solubility in clinopyroxene), the temperature dependence of an increase in $Mg+Fe^{2+}$ in M4 may need revising.

In clinopyroxene, the overestimation of Al and Fe^{3+} appears most closely linked to the charge-balanced substitution $Fe^{3+}Al(iv)$ for MgSi. The augite *a–x* relation does not address this directly, with Fe^{3+} being accommodated in aegirine ($NaFe^{3+}Si_2O_6$), and tetrahedral Al in the Ca-tschermak molecule $CaAl[AlSi]O_6$, with order–disorder over the two tetrahedral sites. Further investigation into the actual ferric iron contents of natural granulite facies clinopyroxene in metabasites will allow a more reliable estimation of the distribution of Fe^{3+} at various peak metamorphic conditions, and possibly provide improvements to the augite *a–x* relation.

6.2 | Implications for modelling high-*T* metabasites

The effect of overestimating Al and underestimating Ca in amphibole is illustrated in ACF diagrams constructed for the amphibolite–granulite facies transition (Figure 15). Tie lines in Figure 15a connect end-member compositions of plagioclase, orthopyroxene, clinopyroxene, and garnet, the latter incorporating a grossular component, with the observed range of hornblende compositions (red ellipse). Figure 15b is the same diagram for the range of calculated hornblende compositions (blue ellipse). Bulk compositions from Table 1 are plotted as green diamonds on Figure 15a,b. For the same bulk composition, the contrasting position of the two hornblende ellipses results in significantly different predicted mineral assemblages or disparate modal proportions for the same mineral assemblage. In Figure 15b (predicted hornblende compositions), the bulk compositions predict smaller modal proportions of hornblende and higher modal proportions of clinopyroxene, than in Figure 15a (observed hornblende compositions). These results match the modal discrepancies noted for samples DWN-346, DWN-362, 87-G-3B, and SA1-13, where the models underestimate the amount of hornblende and overestimate the amount of augite, even when large uncertainties on the bulk composition are considered.

A consequence of the ACF analysis is that the size and position of mineral assemblage stability fields on *P–T* diagrams will be displaced. This in turn may lead to an inaccurate *P–T* estimation based on the comparison of observed mineral modes and compositions with calculated isomode and isopleth lines on phase diagrams. The degree of inaccuracy increases as the modal proportion of hornblende increases, with (1) augite stability progressively expanded to more bulk compositions and to a wider range of *P–T* space, (2) augite being overestimated across phase diagrams, and (3) hornblende being underpredicted across phase diagrams. Point (1) is illustrated in the modelling completed for 87-G-3B, in which the reference *P–T* likely lies at a higher pressure than estimated by previous workers, due to pressure having to exceed the stability field (mode-zero line) for augite to satisfy the observed mineral assemblage (Figure 5a). Examination of the modal abundance predictions for DWN-346 or SA1-13 (Figures 3c and 7c), demonstrates how determining *P–T* conditions using modal isolines for hornblende and clinopyroxene may give inaccurate *P–T* estimates, as a result of points (2) and (3). Moreover, for hornblende-rich samples, the calculated Si-poor hornblende composition may lead to predictions of silica, and thus quartz, oversaturation. An example might be hornblende-rich sample SA1-13 from Kapuskasing, where quartz is predicted to persist above the solidus. This case where "a mineral that would be present only in a minor amount is either present when it should not be, or absent when it should be" (Powell & Holland, 2008, p. 166) has also been suggested for eclogites, with inappropriate thermodynamic models identified as a possible cause (Powell & Holland, 2008). There is no doubt that the successful modelling of high-*T* metabasic systems presents a significant challenge. The current data set and models presented by Green et al. (2016) provides a framework for the distribution of

assemblages in *P–T* space. However, the ultimate goal of performing thermobarometry by matching phase compositions in metabasic rocks will require further development, and this may be assisted by investigating well-equilibrated samples that show a spread of bulk compositions and cover a range of independently constrained *P–T* conditions.

ACKNOWLEDGEMENTS

We acknowledge E. Hansen for the original sample collection at Cone Peak; J. Wade for providing instruction in the use of the department's electron microprobe and scanning electron microscope; and P. Starr for his stimulating discussion with regard to amphibole stoichiometry and bulk rock $X_{Fe^{3+}}$ contents. J. Diener and E. Green are thanked for their insightful and constructive reviews, and R. White for his editorial handling.

REFERENCES

Brown, M. (2007). Crustal melting and melt extraction, ascent and emplacement in orogens: Mechanisms and consequences. *Journal of the Geological Society*, *164*(4), 709–730. https://doi.org/10.1144/0016-76492006-171

Brown, M. (2013). Granite: From genesis to emplacement. *Bulletin of the Geological Society of America*, *125*, 1079–1113. https://doi.org/10.1130/B30877.1

Brown, G. C., & Fyfe, W. S. (1970). The production of granitic melts during ultrametamorphism. *Contributions to Mineralogy and Petrology*, *28*(4), 310–318. https://doi.org/10.1007/BF00388953

Carson, C. J., Powell, R., & Clarke, G. (1999). Calculated mineral equilibria for eclogites in $CaO–Na_2O–FeO–MgO–Al_2O_3–SiO_2–H_2O$: Application to the Pou′ebo Terrane, Pam Peninsula, New Caledonia. *Journal of Metamorphic Geology*, *17*, 9–24. https://doi.org/10.1046/j.1525-1314.1999.00177.x

Colliston, W. P., Schoch, A. E., & Cole, J. (2014). The Grenvillian Namaqua-Natal fold belt adjacent to the Kaapvaal Craton: 1. Distribution of Mesoproterozoic collisional terranes deduced from results of regional surveys and selected profiles in the western and southern parts of the fold belt. *Journal of African Earth Sciences*, *100*, 7–19. https://doi.org/10.1016/j.jafrearsci.2014.05.017

Compton, R. R. (1960). Charnockitic rocks of Santa Lucia Range, California. *American Journal of Science*, *258*(1), 609–636. https://doi.org/10.2475/ajs.258.9.609

Compton, R. R. (1966). Granitic and metamorphic rocks of the Salinian block, California Coast Ranges. *California Division of Mines and Geology Bulletin*, *190*, 277–287.

Cosca, M. A., Essene, E. J., & Bowman, J. R. (1991). Complete chemical analyses of metamorphic hornblendes: Implications for normalizations, calculated H_2O activities, and thermobarometry. *Contributions to Mineralogy and Petrology*, *108*(4), 472–484. https://doi.org/10.1007/BF00303451

Daczko, N. R., Clarke, G. L., & Klepeis, K. A. (2001). Transformation of two-pyroxene hornblende granulite to garnet granulite involving simultaneous melting and fracturing of the lower crust, Fiordland, New Zealand. *Journal of Metamorphic Geology*, *19*, 547–560. https://doi.org/10.1046/j.0263-4929.2001.00328.x

Dale, J., Powell, R., White, R. W., Elmer, F. L., & Holland, T. J. B. (2005). A thermodynamic model for Ca-Na clinoamphiboles in $Na_2O–CaO–FeO–MgO–Al_2O_3–SiO_2–H_2O–O$ for petrological calculations. *Journal of Metamorphic Geology*, *23*(8), 771–791. https://doi.org/10.1111/j.1525-1314.2005.00609.x

Diener, J. F. A., & Powell, R. (2012). Revised activity-composition models for clinopyroxene and amphibole. *Journal of Metamorphic Geology*, *30*(2), 131–142. https://doi.org/10.1111/j.1525-1314.2011.00959.x

Diener, J. F. A., Powell, R., White, R. W., & Holland, T. J. B. (2007). A new thermodynamic model for clino- and orthoamphiboles in the system $Na_2O-CaO-FeO-MgO-Al_2O_3-SiO_2-H_2O-O$. *Journal of Metamorphic Geology*, *25*(6), 631–656. https://doi.org/10.1111/j.1525-1314.2007.00720.x

Diener, J. F. A., White, R. W., & Hudson, T. J. M. (2014). Melt production, redistribution and accumulation in mid-crustal source rocks, with implications for crustal-scale melt transfer. *Lithos*, *200–201*, 212–225. https://doi.org/10.1016/j.lithos.2014.04.021

Droop, G. (1987). A general equation for estimating Fe^{3+} concentrations in ferromagnesian silicates and oxides from microprobe analyses, using stoichiometric criteria. *Mineralogical Magazine*, *51*(361), 431–435. https://doi.org/10.1180/minmag.1987.051.361.10

England, P. C., & Thompson, A. (1986). Some thermal and tectonic models for crustal melting in continental collision zones. *Geological Society, London, Special Publications*, *19*(1), 83–94.

Eskola, P. (1920). The mineral facies of rocks. *Norsk Geologisk Tidsskrift*, *6*, 143–194.

Feisel, Y., White, R. W., Palin, R. M., & Johnson, T. E. (2018). New constraints on granulite facies metamorphism and melt production in the Lewisian Complex, northwest Scotland. *Journal of Metamorphic Geology*, *36*, 1–21. https://doi.org/10.1111/jmg.12311

Frost, R. B., & Chacko, T. (1989). The granulite uncertainty principle: Limitations on thermobarometry in granulites. *Journal of Geology*, *97*, 435–450. https://doi.org/10.1086/629321

Green, E. C. R., White, R. W., Diener, J. F. A., Powell, R., Holland, T. J. B., & Palin, R. M. (2016). Activity-composition relations for the calculation of partial melting equilibria in metabasic rocks. *Journal of Metamorphic Geology*, *34*, 1–25. https://doi.org/10.1111/jmg.12211

Guevara, V. E., & Caddick, M. J. (2016). Shooting at a moving target: Phase equilibria modelling of high-temperature metamorphism. *Journal of Metamorphic Geology*, *34*, 209–235. https://doi.org/10.1111/jmg.12179

Guidotti, C. V., & Dyar, M. D. (1991). Ferric iron in metamorphic biotite and its petrologic and crystallochemical implications. *American Mineralogist*, *76*(1–2), 161–175.

Hansen, E. C., & Harlov, D. E. (2009). Orthophosphate and biotite chemistry from orthopyroxene-bearing migmatites from California and South India: The role of a fluid-phase in the evolution of granulite-facies migmatites. *Mineralogy and Petrology*, *95*(3–4), 201–217. https://doi.org/10.1007/s00710-008-0033-2

Hansen, E., & Stuk, M. (1993). Orthopyroxene-bearing, mafic migmatites at Cone Peak, California: Evidence for the formation of migmatitic granulites by anatexis in an open system. *Journal of Metamorphic Geology*, *11*(1993), 291–307. https://doi.org/10.1111/j.1525-1314.1993.tb00148.x

Hartel, T. H. D., & Pattison, D. R. M. (1996). Genesis of the Kapuskasing (Ontario) migmatitic mafic granulites by dehydration melting of amphibolite: The importance of quartz to reaction progress. *Journal of Metamorphic Geology*, *14*(5), 591–611. https://doi.org/10.1046/j.1525-1314.1996.00404.x

Hartnady, C., Joubert, P., & Stowe, C. (1985). Proterozoic crustal evolution in Southwestern Africa. *Episodes*, *8*(4), 236–244.

Haynes, J. (1998). *Processes of granulite formation, West Greenland*. Unpublished doctoral dissertation, University of Oxford.

Holland, T. J. B., & Blundy, J. (1994). Non-ideal interactions in calcic amphiboles and their bearing on amphibole-plagioclase thermometry. *Contributions to Mineralogy and Petrology*, *116*(4), 433–447. https://doi.org/10.1007/BF00310910

Holland, T. J. B., & Powell, R. (1998). An internally consistent thermodynamic data set for phases of petrological interest. *Journal of Metamorphic Geology*, *16*(3), 309–343. https://doi.org/10.1111/j.1525-1314.1998.00140.x

Holland, T. J. B., & Powell, R. (2003). Activity-compositions relations for phases in petrological calculations: An asymetric multicomponent formulation. *Contributions to Mineralogy and Petrology*, *145*(4), 492–501. https://doi.org/10.1007/s00410-003-0464-z

Holland, T. J. B., & Powell, R. (2011). An improved and extended internally consistent thermodynamic dataset for phases of petrological interest, involving a new equation of state for solids. *Journal of Metamorphic Geology*, *29*(3), 333–383. https://doi.org/10.1111/j.1525-1314.2010.00923.x

Huang, G., Brown, M., Guo, J., Piccoli, P., & Zhang, D. (2018). Challenges in constraining the P-T conditions of mafic granulites: An example from the northern Trans-North China Orogen. *Journal of Metamorphic Geology*, https://doi.org/10.1111/jmg.12308

Janardhan, A. S., Newton, R. C., & Hansen, E. C. (1982). The transformation of amphibolite facies gneiss to charnockite in southern Karnataka and northern Tamil Nadu, India. *Contributions to Mineralogy and Petrology*, *79*(2), 130–149. https://doi.org/10.1007/BF01132883

Johnson, T. E., & White, R. W. (2011). Phase equilibrium constraints on conditions of granulite-facies metamorphism at Scourie, NW Scotland. *Journal of the Geological Society*, *168*(1), 147–158. https://doi.org/10.1144/0016-76492010-069

Kidder, S., Ducea, M., Gehrels, G., Patchett, P. J., & Vervoort, J. (2003). Tectonic and magmatic development of the Salinian Coast Ridge Belt, California. *Tectonics*, *22*(5), 1058–1078. https://doi.org/10.1029/2002TC001409

Krogh, T. E. (1993). High precision U-Pb ages for granulite metamorphism and deformation in the Archean Kapuskasing structural zone, Ontario: Implications for structure and development of the lower crust. *Earth and Planetary Science Letters*, *119*, 1–18. https://doi.org/10.1016/0012-821X(93)90002-Q

Kumar, C. R. R., & Chacko, T. (1994). Geothermobarometry of mafic granulites and metapelite from the Palghat Gap, South India: Petrological evidence for isothermal uplift and rapid cooling. *Journal of Metamorphic Geology*, *12*(4), 479–492. https://doi.org/10.1111/j.1525-1314.1994.tb00037.x

Leake, B. E., Woolley, A. R., Arps, C., Birch, W. D., Gilbert, M. C., Grice, J. D., … Krivovichev, V. G. (1997). Nomenclature of amphiboles: Report of the subcommittee on amphiboles of the International Mineralogical Association Commission on New Minerals and Mineral Names. *Canadian Mineralogist*, *35*(6), 219–246. https://doi.org/10.1180/minmag.1997.061.405.13

Leake, B. E., Woolley, A. R., Birch, W. D., Burke, E. A., Ferraris, G., Grice, J. D., … Whittaker, E. J. (2003). Nomenclature of amphiboles: Additions and revisions to the International Mineralogical Association's 1997 recommendations. *The Canadian Mineralogist*, *41*, 1355–1362. https://doi.org/10.2113/gscanmin.41.6.1355

Loock, G., Stosch, H. G., & Seck, H. A. (1990). Granulite facies lower crustal xenoliths from the Eifel, West Germany: Petrological and geochemical aspects. *Contributions to Mineralogy and Petrology*, *105*(1), 25–41. https://doi.org/10.1007/BF00320964

Loucks, R. R. (1990). Discrimination of ophiolitic from nonophiolitic ultramafic-mafic allochthons in orogenic belts by the Al/Ti ratio in clinopyroxene. *Geology*, *18*(4), 346–349. https://doi.org/10.1130/0091-7613(1990) 018<0346:DOOFNU>2.3.CO;24

Love, G. J., Kinny, P. D., & Friend, C. R. L. (2004). Timing of magmatism and metamorphism in the Gruinard Bay area of the Lewisian Gneiss Complex: Comparisons with the Assynt Terrane and implications for terrane accretion. *Contributions to Mineralogy and Petrology*, *146*(5), 620–636. https://doi.org/10.1007/s00410-003-0519-1

Mason, A., & Brewer, T. (2005). A re-evaluation of a Laxfordian terrane boundary in the Lewisian complex of south Harris, NW Scotland. *Journal of the Geological Society*, *162*(2004), 401–407. https://doi.org/10.1144/0016-764904-050

Mattinson, J. M. (1978). Age, origin, and thermal histories of some plutonic rocks from the Salinian block of California. *Contributions to Mineralogy and Petrology*, *67*(3), 233–245. https://doi.org/10.1007/BF00381451

McStay, J. (1991). *Granulite-facies metamorphism, fluid buffering and partial melting in the Buffels River area of the Namaqualand Metamorphic Complex, South Africa*. Unpublished doctoral dissertation, University of Cape Town.

Morimoto, N. (1988). Nomenclature of pyroxenes. *Mineralogical Magazine*, *52*, 535–550. https://doi.org/10.1180/minmag.1988.052.367.15

Newton, R. C., Smith, J. V., & Windley, B. F. (1980). Carbonic metamorphism, granulites and crustal growth. *Nature*, *288*(5786), 45–50

Palin, R. M., Weller, O. M., Waters, D. J., & Dyck, B. (2016). Quantifying geological uncertainty in metamorphic phase equilibria modelling: A Monte Carlo assessment and implications for tectonic interpretations. *Geoscience Frontiers*, *7*(4), 591–607. https://doi.org/10.1016/j.gsf.2015.08.005

Palin, R. M., White, R. W., Green, E. C. R., Diener, J. F. A., Powell, R., & Holland, T. J. B. (2016). High-grade metamorphism and partial melting of basic and intermediate rocks. *Journal of Metamorphic Geology*, *34*, 1–22. https://doi.org/10.1111/jmg.12212

Park, R. G. (1966). Nature and origin of Lewisian basic rocks of Gairloch, Ross-shire. *Scottish Journal of Geology*, *2*, 179–199. https://doi.org/10.1144/sjg02020179

Patiño Douce, A. E. & Beard, J. S. (1995). Dehydrations-melting of biotite gneiss and quartz amphibolite from 3 to 15 kbar. *Journal of Petrology*, *36*(3), 707–738. https://doi.org/10.1093/petrology/36.3.707

Pattison, D. R. M. (1991). Infiltration-driven dehydration and anatexis in granulite facies metagabbro, Grenville Province, Ontario, Canada. *Journal of Metamorphic Geology*, *9*(3), 315–332. https://doi.org/10.1111/j.1525-1314.1991.tb00526.x

Pattison, D. R. M., & Bègin, N. J. (1994). Zoning patterns in orthopyroxene and garnet in granulites: Implications for geothermometry. *Journal of Metamorphic Geology*, *12*(4), 387–410. https://doi.org/10.1111/j.1525-1314.1994.tb00031.x

Pattison, D. R. M., Chacko, T., Farquhar, J., & McFarlane, C. R. M. (2003). Temperatures of granulite-facies metamorphism:

Constraints from experimental phase equilibria and thermobarometry corrected for retrograde exchange. *Journal of Petrology*, *44*(5), 867–900. https://doi.org/10.1093/petrology/44.5.867

Peach, B. N., Horne, J., Gunn, W., Clough, C. T., Hinxman, L. W., & Teall, J. J. H. (1907). *The geological structure of the North-West highlands of Scotland*. Glasgow, UK: HM Stationery Office.

Percival, J. A. (1983). High-grade metamorphism in the Chapleau-Foleyet Area, Ontario. *American Mineralogist*, *68*, 667–686.

Percival, J. A., & Card, K. (1983). Archean crust as revealed in the Kauskasing uplift, Superior province Canada. *Geology*, *11*, 323–326. https://doi.org/10.1130/0091-7613(1983)11<323:ACARIT>2.0.CO;2

Popp, R. K., & Bryndzia, L. T. (1992). Statistical analysis of Fe^{3+}, Ti, and OH in kaersutite from alkalic igneous rocks and mafic mantle xenoliths. *American Mineralogist*, *77*(11–12), 1250–1257.

Powell, R., & Holland, T. J. B. (1988). An internally consistent dataset with uncertainties and correlations: 3. Applications to geobarometry, worked examples and a computer program. *Journal of Metamorphic Geology*, *6*(2), 173–204. https://doi.org/10.1111/j.1525-1314.1988.tb00415.x

Powell, R., & Holland, T. J. B. (1994). Optimal geothermometry and geobarometry. *American Mineralogist*, *79*(1–2), 120–133.

Powell, R., & Holland, T. J. B. (2008). On thermobarometry. *Journal of Metamorphic Geology*, *26*, 155–179. https://doi.org/10.1111/j.1525-1314.2007.00756.x

Powell, R., Holland, T. J. B., & Worley, B. A. (1998). Calculating phase diagrams involving solid solutions via non-linear equations, with examples using THERMOCALC. *Journal of Metamorphic Geology*, *16*, 577–588. https://doi.org/10.1111/j.1525-1314.1998.00157.x

Robb, L. J., Armstrong, R. A., & Waters, D. J. (1999). The history of granulite-facies metamorphism and crustal growth from single zircon U-Pb geochronology: Namaqualand, South Africa. *Journal of Petrology*, *40*(12), 1747–1770. https://doi.org/10.1093/petroj/40.12.1747

Roduit, N. (2016). JMicroVision: Image analysis toolbox for measuring and quantifying components of high-definition images. Retrieved from http://www.jmicrovision.com/

Rollinson, H. R., & Fowler, M. B. (1987). The magmatic evolution of the Scourian complex at Gruinard Bay. *Geological Society, London, Special Publications*, *27*(1), 57–71.

Rollinson, H. R., & Windley, B. F. (1980). Mineralogy and selective elemental depletion during metamorphism in granulites. *Contributions to Mineralogy and Petrology*, *72*, 257–263.

Ross, D. C. (1976). Distribution of metamorphic rocks and mineral occurrences, Santa Lucia Range, California. US Geological Survey, Miscellane (MF-191).

Sawyer, E. W. (1994). Melt segregation in the continental crust. *Geology*, *22*, 1019–1022. https://doi.org/10.1130/0091-7613

Sawyer, E. W. (2001). Melt segregation in the continental crust: Distribution and movement of melt in anatectic rocks. *Journal of Metamorphic Geology*, *19*, 291–309. https://doi.org/10.1046/j.0263-4929.2000.00312.x

Schumacher, J. C. (2007). Metamorphic amphiboles: Composition and coexistence. *Reviews in Mineralogy and Geochemistry*, *67*(1), 359–416. https://doi.org/10.2138/rmg.2007.67.10

Sills, J. D., & Rollinson, H. R. (1987). Metamorphic evolution of the mainland Lewisian complex. *Geological Society, London, Special Publications*, *27*(1), 81–92.

Spear, F. S. (1993). *Metamorphic phase equilibria and pressure-temperature-time paths*. Washington, DC: Mineralogical Society of America.

Stüwe, K., & Powell, R. (1995). P–T paths from modal proportions: Application to the Koralm Complex, Eastern Alps. *Contributions to Mineralogy and Petrology*, *119*, 83–93. https://doi.org/10.1007/bf00310719 https://doi.org/10.1007/BF00310719

Van der Plas, L. V. D., & Tobi, A. C. (1965). A chart for judging the reliability of point counting results. *American Journal of Science*, *263*(1), 87–90. https://doi.org/10.2475/ajs.263.8.722

Waters, D. J. (1988). Partial melting and the formation of granulite facies assemblages in Namaqualand, South Africa. *Journal of Metamorphic Geology*, *6*, 387–404. https://doi.org/10.1111/j.1525-1314.1988.tb00430.x

Waters, D. J. (1989). Metamorphic evidence for the heating and cooling path of Namaqualand granulites. *Geological Society, London, Special Publications*, *43*(1), 357–363.

Waters, D. J., & Charnley, N. R. (2002). Local equilibrium in polymetamorphic gneiss and the titanium substitution in biotite. *American Mineralogist*, *87*(4), 383–396. https://doi.org/10.2138/am-2002-0402

Waters, D. J., & Moore, J. M. (1985). Kornerupine in Mg-Al-rich gneisses from Namaqualand, South Africa: Mineralogy and evidence for late-metamorphic fluid activity. *Contributions to Mineralogy and Petrology*, *91*(4), 369–382. https://doi.org/10.1007/BF00374693

White, R. W., Palin, R. M., & Green, E. C. R. (2017). High-grade metamorphism and partial melting in Archean composite grey gneiss complexes. *Journal of Metamorphic Geology*, *35*, 181–195. https://doi.org/10.1111/jmg.12227

White, R. W., Powell, R., & Clarke, G. L. (2002). The interpretation of reaction textures in Fe-rich metapelitic granulites of the Musgrave Block, Central Australia: Constraints from mineral equilibria calculations in the system. *Journal of Metamorphic Geology*, *20*(1), 41–55. https://doi.org/10.1046/j.0263-4929.2001.00349.x

White, R. W., Powell, R., Holland, T. J. B., Johnson, T. E., & Green, E. C. R. (2014). New mineral activity-composition relations for thermodynamic calculations in metapelitic systems. *Journal of Metamorphic Geology*, *32*(3), 261–286. https://doi.org/10.1111/jmg.12071

White, R. W., Powell, R., Holland, T. J. B., & Worley, B. A. (2000). The effect of TiO_2 and Fe_2O_3 on metapelitic assemblages at greenschist and amphibolite facies conditions: Mineral equilibria calculations in the system K_2O–FeO–MgO–Al_2O_3–SiO_2–H_2O–TiO_2–Fe_2O_3. *Journal of Metamorphic Geology*, *18*, 497–511. https://doi.org/10.1046/j.1525-1314.2000.00269.x

Zhao, G. C., Wilde, S. A., Cawood, P. A., & Liu, L. Z. (2000). Petrology and P-T path of the Fuping mafic granulites: Implications for tectonic evolution of the central zone of the North China craton. *Journal of Metamorphic Geology*, *18*, 375–391. https://doi.org/10.1046/j.1525-1314.2000.00264.x

SUPPORTING INFORMATION

Additional supporting information may be found online in the Supporting Information section at the end of the article.

Table S1. Mean weight per cent oxide analyses of plagioclase, in all six samples, with cations calculated for an 8-oxygen formula unit. For analyses collected in this study, the spread is expressed as 2 *SD*s about the mean.

Table S2. Mean weight per cent oxide analyses of hornblende, in all six samples, with cations calculated for a 23-oxygen+Ti cations/2 formula unit. For analyses collected in this study, the spread is expressed as 2 *SD*s about the mean.

Table S3. Mean weight per cent oxide analyses of clinopyroxene, in the five augite-bearing samples, with cations calculated for a 6-oxygen formula unit. For analyses collected in this study, the spread is expressed as 2 *SD*s about the mean.

Table S4. Mean weight per cent oxide analyses of orthopyroxene in DWN-346, DWN-362, and S98-15, with cations calculated for a 6-oxygen formula unit. The spread in analyses is expressed as 2 *SD*s about the mean.

Table S5. Mean weight per cent oxide analyses of garnet in 87-G-3B, SA1-13, and SA1-4a, with cations calculated for a 12-oxygen formula unit. For analyses collected in this study, the spread is expressed as 2 *SD*s about the mean.

Table S6. Mean weight per cent oxide analyses of biotite in DWN-346, 87-G-3B, and S98-15, with cations calculated for a 22-oxygen+Ti cations formula unit. The spread of analyses for 87-G-3B and S98-15 is expressed as 2 *SD*s about the mean; no *SD*s are quoted for DWN-346 since very little biotite is present in the rock and therefore only a few analyses were made.

Table S7. Observed (Obs) and calculated (Calc) modal phase proportions (vol.%) for each sample, determined at the reference *P–T* conditions referred to in the text.

How to cite this article: Forshaw JB, Waters DJ, Pattison DRM, Palin RM, Gopon P. A comparison of observed and thermodynamically predicted phase equilibria and mineral compositions in mafic granulites. *J Metamorph Geol*. 2018;00:1–27. https://doi.org/10.1111/jmg.12454